

Manuscript Number: AES2122

Title: Thermodynamic modelling of Sol Hamed serpentinite, South Eastern Desert of Egypt: implication for fluid interaction in the Arabian-Nubian Shield ophiolites

Article Type: Research Paper

Keywords: Arabian-Nubian Shield; Forearc peridotite; Ophiolites; Carbonatization; Thermodynamic modelling; T-XCO₂

Abstract: The Arabian-Nubian Shield is the largest tract of juvenile continental crust of the Neoproterozoic. This crust was generated due to arc-arc collision associated with the closing of the Mozambique Ocean, and ophiolitic rocks mark suture zones in the shield. The Sol Hamed ophiolite in the southeastern Egypt defines a near-source tectonic facies, representing an uncommon example of rocks that might be less deformed due to the movement far from the corresponding suture. In order to understand fluid-rock interactions before and during arc-arc collision, petrological, mineral chemistry, whole-rock chemistry and thermodynamic studies were applied to the Sol Hamed serpentinitized ophiolitic mantle fragment. These studies reveal that the protolith had a harzburgite composition that probably originated as forearc mantle. Protolith alteration resulted from two stages of fluid-rock interaction. The first stage occurred as a result of infiltration of concentrated CO₂-rich fluid released from carbonate bearing sediments and altered basalt at the subduction zone. The alteration occurred during isobaric cooling at a pressure of 1 kbar. The fluid composition during the isobaric cooling was buffered by the metamorphic reactions. The second stage of fluid-rock interactions took place through prograde metamorphism. The increase in pressure during this stage occurred as a result of thrusting within the oceanic crust. In this process the forearc crust was loaded by roughly 20-30 km of overthrust rocks.

Abstract

The Arabian-Nubian Shield is the largest tract of juvenile continental crust of the Neoproterozoic. This crust was generated due to arc-arc collision associated with the closing of the Mozambique Ocean, and ophiolitic rocks mark suture zones in the shield. The Sol Hamed ophiolite in the southeastern Egypt defines a near-source tectonic facies, representing an uncommon example of rocks that might be less deformed due to the movement far from the corresponding suture. In order to understand fluid-rock interactions before and during arc-arc collision, petrological, mineral chemistry, whole-rock chemistry and thermodynamic studies were applied to the Sol Hamed serpentinitized ophiolitic mantle fragment. These studies reveal that the protolith had a harzburgite composition that probably originated as forearc mantle. Protolith alteration resulted from two stages of fluid-rock interaction. The first stage occurred as a result of infiltration of concentrated CO₂-rich fluid released from carbonate bearing sediments and altered basalt at the subduction zone. The alteration occurred during isobaric cooling at a pressure of 1 kbar. The fluid composition during the isobaric cooling was buffered by the metamorphic reactions. The second stage of fluid-rock interactions took place through prograde metamorphism. The increase in pressure during this stage occurred as a result of thrusting within the oceanic crust. In this process the forearc crust was loaded by roughly 20-30 km of overthrust rocks.

1
2
3
4
5
6
7
8
9
10
11
12
13
14
15
16
17
18
19
20
21
22
23
24
25
26
27
28
29
30
31
32
33
34
35
36
37
38
39
40
41
42
43
44
45
46
47
48
49
50
51
52
53
54
55
56
57
58
59
60
61
62
63
64
65

- Sol Hamed ophiolitic has a harzburgite composition as protolith
- The protolith originated as forearc mantle
- Protolith alteration resulted from two stages of fluid-rock interaction
- First stage is due to infiltration of CO₂-rich fluid during isobaric cooling
- Second stage of fluid-rock interactions took place through prograde metamorphism

1
2
3
4
5
6
7
8
9
10
11
12
13
14
15
16
17
18
19
20
21
22
23
24

**Thermodynamic modelling of Sol Hamed serpentinite, South Eastern Desert of
Egypt: implication for fluid interaction in the Arabian-Nubian Shield ophiolites**

T. S. Abu-Alam^{1,2} and M. M. Hamdy¹

1 Geology Department, Faculty of Science, Tanta University, Tanta, Egypt

2 Institut für Erdwissenschaften, Universität Graz, Universitätsplatz 2, A-8010 GRAZ,
Austria

Corresponding author: T.S. Abu-Alam (tamer.abu-alam@uni-graz.at)

Short title: Fluid interaction in the Arabian-Nubian Shield ophiolites

25 **Abstract**

26

27 The Arabian-Nubian Shield is the largest tract of juvenile continental crust of the
28 Neoproterozoic. This crust was generated due to arc-arc collision associated with the
29 closing of the Mozambique Ocean, and ophiolitic rocks mark suture zones in the shield.
30 The Sol Hamed ophiolite in the southeastern Egypt defines a near-source tectonic facies,
31 representing an uncommon example of rocks that might be less deformed due to the
32 movement far from the corresponding suture. In order to understand fluid-rock
33 interactions before and during arc-arc collision, petrological, mineral chemistry, whole-
34 rock chemistry and thermodynamic studies were applied to the Sol Hamed serpentinized
35 ophiolitic mantle fragment. These studies reveal that the protolith had a harzburgite
36 composition that probably originated as forearc mantle. Protolith alteration resulted from
37 two stages of fluid-rock interaction. The first stage occurred as a result of infiltration of
38 concentrated CO₂-rich fluid released from carbonate bearing sediments and altered basalt
39 at the subduction zone. The alteration occurred during isobaric cooling at a pressure of 1
40 kbar. The fluid composition during the isobaric cooling was buffered by the metamorphic
41 reactions. The second stage of fluid-rock interactions took place through prograde
42 metamorphism. The increase in pressure during this stage occurred as a result of thrusting
43 within the oceanic crust. In this process the forearc crust was loaded by roughly 20-30 km
44 of overthrust rocks.

45

46 Key-words: Arabian-Nubian Shield; Forearc peridotite; Ophiolites; Carbonatization;
47 Thermodynamic modelling; *T-XCO₂*.

48 **1. Introduction**

49 Arabian-Nubian Shield (ANS) in Northeast Africa and West Arabia is the largest tract of
50 juvenile continental crust of Neoproterozoic age on Earth (Patchett and Chase 2002;
51 Stern et al. 2004). This crust was generated when arc terranes were created within and
52 around the margins of the Mozambique Ocean, which formed in association with the
53 breakup of Rodinia ~ 800–900 Ma (Stern 1994; Hassan et al. in-review). These crustal
54 fragments collided as the Mozambique Ocean closed around 600 Ma (Meert 2003),
55 forming arc-arc sutures, composite terranes, the Arabian-Nubian Shield (Fig. 1), and the
56 larger collisional belt known as the East-African Orogen (Stern 1994; Kusky et al. 2003,
57 Stern et al. 2004). Due to this collision processes a supercontinent variously referred to as
58 Greater Gondwanaland (Stern 1994), Pannotia (Dalziel 1997) or just Gondwana (e.g.
59 Abu-Alam et al. 2013) was formed.

60 Ophiolitic rocks are remarkably abundant in the ANS. They are scattered across most of
61 the shield, over a distance of ~ 3000 km from the farthest north (Gebel Ess) almost to the
62 equator, and from Rahib in the west to Gebel Uwayjah (45° E) in the east (Fig. 1). The
63 abundance of the ophiolites is a further indication that the Arabian-Nubian Shield was
64 produced by processes similar to those of modern plate tectonics (Stern et al. 2004).

65 The ophiolitic rocks of Eastern Desert (ED) of Egypt (Fig. 1) are interpreted to be formed
66 in a suprasubduction zone (SSZ) (e.g. Ahmed et al. 2006; Azer and Stern 2007) which
67 operated at forearc convergent margin (e.g. Stern et al. 2004; El-Gaby 2005). The East-
68 and West-Gondwana collision led to obduction of the SSZ ophiolitic rocks over a
69 continental margin (Akaad and Abu El Ela 2002; El-Gaby 2005) of the West-Gondwana

70 (Abd El-Rahman et al. 2009). Subduction was active while the process of ophiolitic
71 overthrusting was operative along thrust planes (Kröner et al. 1987; Stern 1994).

72 The ophiolite obduction and overthrusting were associated with fluid-rocks interaction
73 and hence alteration, serpentinization and metasomatism took place (e.g. Hamdy et al.
74 2013) but it is often not known whether this alteration occurred before, during or after the
75 obduction (Stern et al. 2004). On other hand, much doubt exists around origin and
76 composition of the fluid during the alteration process. Some authors suggested that the
77 alteration of ultramafic rocks – the dominant component of the ANS’s ophiolites –
78 occurred by interaction with hot fluid during seafloor weathering (e.g. Lebda 1995; Li
79 and Lee 2006). Other authors believed that the alteration took place by infiltration of
80 metamorphic and hydrothermal fluid along major tectonic fractures during or after rock
81 exhumation (e.g. Hyndman and Peacock 2003; Hamdy 2004; Hamdy and Lebda 2007).

82 Sol Hamed ophiolite in the southeastern Egypt and northeastern Sudan (Fitches et al.
83 1983) differs from other ophiolites further north in the ED of Egypt in being an elongated
84 belt defining a near-source tectonic facies (Abdelsalam and Stern 1996). To the north,
85 ophiolites occur in tectonic mélanges or as olistostromal debris, indicating a distal
86 tectonic facies. This interpretation implies the ophiolitic rocks north of the Sol Hamed
87 represent a far-travelled ophiolitic nappe, transported to the north away from its
88 corresponding suture. Thus the Sol Hamed rocks represent an uncommon example in the
89 Eastern Desert that might be less deformed by the movement along faults that occurred
90 after the closure of the Mozambique Ocean. In this work, petrological relationships,
91 mineral chemistry, geochemistry and thermodynamic modelling are described and
92 applied to rocks from Sol Hamed ophiolite (Fig. 2). The results help to more clearly

93 define the nature of the fluid-rock interactions process occurred in the intraoceanic
94 collision of the ANS.

95

96 **2. Geological setting**

97 Many of the ultramafic outcrops in the Arabian-Nubian Shield are detached, scattered
98 and isolated (Fig. 1) due to intrusion of syn- and post-tectonic plutons. Gass (1977) noted
99 that these ultramafic bodies have tectonic contacts with other Pan-African rocks. Some of
100 these ultramafic are recognized as ophiolites, representing obducted fragments of an
101 oceanic lithosphere that existed between the Proterozoic island arcs (Gareson and
102 Shalaby 1976; El-Ramly et al. 1993). Dixon (1979) estimated that the ultramafic bodies
103 account for 5.3% of all Precambrian outcrops in Egypt. Serpentinized ultramafics
104 constitute the major part of these ophiolite complexes (Ahmed et al. 2001).

105 The Sol Hamed ophiolite is a part of Allaqi-Heiani-Onib-Sol Hamed-Yanbu arc-arc
106 suture (Abdelsalam and Stern 1996; Abdelsalam et al. 2003). This arc-arc suture is
107 considered – along with the Ariab-Nakasib-Thurwah-Bir Umq suture farther south in
108 Arabia and Sudan (Johnson et al. 2004) to be one of the two longest and most complete
109 Neoproterozoic ophiolite-decorated sutures in the ANS (Azer et al. 2013). Stern et al.
110 (1990) proposed that the Allaqi-Heiani-Onib-Sol Hamed-Yanbu suture represents a south
111 verging nappe which was refolded around a subhorizontal east-west trending axes to
112 produce upright antiforms and late-stage southeast verging thrusts. Vergence of the
113 ophiolite nappe was used to infer a north dipping subduction zone along the line of a
114 suture which lies north of the Allaqi-Heiani-Onib-Sol Hamed-Yanbu ophiolite. Ali et al.

115 (2010) suggested two stages for the evolution of Allaqi-Heiani-Onib-Sol Hamed-Yanbu
116 suture (~810–780 Ma and ~750–730 Ma).

117 The ultramafic rocks of Sol Hamed (Fig. 2) are composed of serpentinized peridotite
118 forming the base of a dismembered ophiolitic sequence that comprises also metagabbros,
119 pillow lavas and pelagic sediments (Abu El-Laban 2002). They occur as sheets and lenses
120 enclosed within mélangé matrix comprises island arc volcanosedimentary assemblages,
121 gneiss and syn- to post-orogenic intrusions (e.g. Kröner et al. 1987; Greiling et al. 1988;
122 Taylor et al. 1993; Abd El-Naby and Frisch 2002; Kusky and Ramadan 2002;
123 Abdelsalam et al. 2003; Zoheir and Klemm 2007; Ali et al. 2010). Serpentinized
124 ophiolitic peridotites form ridges about 20 km long and about 0.4–1.8 km wide, elongated
125 in NE-SW direction. They are mostly massive but are sometimes brecciated and
126 fragmented along their contacts with the mélangé matrix. Some portions contain relicts of
127 primary minerals and others are extremely altered, especially along thrusts and shear
128 zones, with the development of talc, talc-carbonate and reddish brown quartz-carbonate
129 rock (listwaenite).

130 Chromitite deposits occur mainly as lenticular bodies of variable dimensions up to 25 m
131 length × 6 m width, trending ENE-WSW. Thick pods are abundant in serpentinites that
132 are mostly derived from dunite. Micro-lenses and thin planar segregations occur in the
133 serpentinized peridotite. Gradual contacts between massive ore and serpentinized dunite
134 over a meter-range are frequently observed. A typical contact shows gradation from fine-
135 grained disseminated chromite in the dunite through nodular, to massive coarse-grained
136 chromite ore. The highly deformed chromite bodies are the most abundant. Magnesite
137 veins occur in shear zones close to the eastern periphery of the serpentinite rocks. Hamdy

138 (2007) based on the C-O isotopes of these veins estimated that carbon was supplied from
139 both geothermal fluids (giving magnesite with $\delta^{13}\text{C}$ values from -2.06 to -4.34% VPDB)
140 and metamorphic carbonaceous sediments (giving magnesite with $\delta^{13}\text{C}$ values from -9.44
141 to -10% VPDB).

142

143 **3. Petrography**

144 Variable degrees of alterations are observed in the studied ultramafic rocks. Original
145 peridotite minerals have been preserved (Table 1) in partly altered peridotites. The
146 dominant serpentine mineral is lizardite, whereas chrysotile is subordinate. The lizardite
147 forms pseudomorphic mesh and bastite textures after olivine and orthopyroxene and
148 sometimes occurs as interlocking and penetrating grains (non-pseudomorphic). The
149 chrysotile occurs as cross fiber veins traversing the lizardite matrix. Serpentine minerals
150 appear to be accompanied by shedding of fine-grained magnetite, which concentrates in
151 veins cutting zoned chromite (Fig. 3a) or along relict pyroxene cleavages. Pyroxene
152 relicts occur as inclusions in anthophyllite (Fig. 3a). The anthophyllite is a common
153 replacement mineral of orthopyroxene, where it initially grows along cleavage planes and
154 eventually replaces the whole grain. Talc is not abundant in the studied serpentinites. It
155 forms fine shreds, dense fibers and medium grained flaky crystals (0.01–0.04 mm).
156 Perfect cleavage, straight extinction and high interference colours are characteristic
157 features of the talc. The talc is pseudomorphic after anthophyllite. It is homogenous and
158 commonly associated with the alteration of orthopyroxene. All serpentinite samples
159 contain zoned-chromite (Fig. 3b) and sulphide grains. Chromite occurs as disseminated

160 subhedral and anhedral crystals of reddish brown colour. Some chromite grains look
161 homogeneous in reflected light.

162

163 **4. Mineral chemistry**

164 Different mineral phases were examined in the Institute of Geological Sciences of Polish
165 Academy of Sciences (IGS-PAS). The electron microprobe analyses were carried out by
166 JEOL-JXA-840A scanning electron microscope equipped with Link Analytical AN-
167 1000/855 energy dispersive X-ray spectrometer. The analytical conditions were 15 kV
168 accelerating voltage and 35 nA beam current. Mineral formula and activity of the end-
169 members were calculated by AX program ([http://www.esc.cam.ac.uk/research/research-](http://www.esc.cam.ac.uk/research/research-groups/holland/ax)
170 [groups/holland/ax](http://www.esc.cam.ac.uk/research/research-groups/holland/ax)). The chemical formula of the serpentine minerals was calculated
171 based on 28 oxygen atoms and ignoring the H₂O, pyroxene formula based on 6 oxygen
172 atoms. 11 oxygen atoms and ignoring the H₂O were used to calculate talc formula, 24
173 oxygen atoms were used for the spinel while the carbonate formula was calculated based
174 on 2 cations. The mineral abbreviations which will be used in the following sections are
175 from Holland and Powell (2011).

176 CaO content is below 0.03 wt% in the orthopyroxene and FeO content is in the range of
177 4.85 – 5.09 wt% while MgO content is around 35 wt% (Table 2). This reveals that the
178 main pyroxene end-member is enstatite. SiO₂ content of the serpentine ranges between
179 40.62 and 44.54 (Table 2). Al₂O₃ is in the range of below the detection limit up to 1.79
180 wt%. FeO shows a wide range (0.83 – 6.21 wt%). MgO ranges between 34.37 to 39.35
181 wt%. The MgO and the FeO ranges indicate ionic substitution between Fe²⁺ and Mg²⁺.
182 Figure 4a shows limitation of the substitution between Al³⁺, Mg²⁺ and Si⁴⁺ in the

183 serpentine crystals. FeO and Cr₂O₃ contents in lizardite increase (0.94 to 6.21 wt% and
184 from below detection limit to 0.36 wt% for FeO and Cr₂O₃, respectively) distinctly with
185 increasing degree of alteration from partly to completely serpentinized rocks (Table 2).
186 Chrysotile shows that Al and Cr are relatively immobile during recrystallization of
187 lizardite and therefore remain in their original crystal lattice.

188 Low Al₂O₃ and TiO₂ contents in talc chemistry reveal limitation in substitution between
189 Si, Ti and Al. The main ionic substitution is between Mg²⁺ and Fe²⁺ (Table 3). The
190 activities of talc and Fe-talc end-members are in the range of 0.68-0.85 and 0.00013-
191 0.00061, respectively. Table (4) shows chemical analyses of the carbonate minerals. The
192 high concentrations of MgO and FeO (35.53-40.14 and 8.46-14.1 wt%, respectively)
193 indicate high activity of the magnesite and the siderite end-members. The CaO content is
194 in the range of 0.04 to 0.27 wt% revealing low activity of the calcite.

195 Three compositional zones are distinguished for the spinel minerals. The composition of
196 core, intermediate and rim zones is given in Table (5) and plotted in Al-Cr-Fe³⁺ triangle
197 of Stevens (1944) (Fig. 4b). Cores and intermediates zones have aluminian chromite to
198 ferritchromite composition. Composition of the outer rim is Cr-magnetite which is nearly
199 devoid of Al and lie along the Cr-Fe³⁺ sideline (Fig. 4b). The studied spinels show
200 metamorphic conditions correspond to that of the upper greenschist to the transitional
201 greenschist-amphibolite facies (Fig. 4b).

202 The variation in the spinel composition can be interpreted as a result of chemical
203 alteration under hydrothermal conditions (Abzalov 1998; Barnes 2000; Proenza et al.
204 2004). The alteration is accompanied by decrease in Al, Mg and Cr contents and
205 consequence increase in Fe³⁺ and Fe²⁺. Apparently with the increasing of the alteration,

206 Fe releases from olivine and orthopyroxene and Cr releases from chromite and are
207 accommodated in the serpentines. In addition, the wide compositional variation
208 (particularly in Al_2O_3) reflects temporal and/or spatial variations in melt types (boninitic
209 and tholeiitic) that were generated from, and emplaced in subarc mantle domains in a
210 suprasubduction zone environment (Hamdy and Lebda 2011).

211

212 **5. Whole-rock chemistry**

213 Representative bulk rock chemistry of Sol Hamed serpentinite is given in Table (6).
214 Chemical analyses of major and some trace elements were carried out at the
215 geochemistry laboratory of the IGS-PAS. Concentrations of major and trace elements were
216 determined after microwave-assisted acid digestion with atomic absorption
217 spectrophotometer (AAS-PU 9100xUNICAM). Before digestion samples were heated to
218 1100 to determine loss on ignition (LOI). Analytical precession was better than 0.5% for
219 major elements and 4 ppm for trace elements.

220 Due to the almost complete serpentinization of some of the Sol Hamed peridotites, modal
221 compositions could not be determined. Therefore, normative compositions were
222 calculated from anhydrous analyses using the CIPW norm, assuming a $\text{Fe}_2\text{O}_3/\text{FeO}$ ratio
223 of 0.2 (Melcher et al. 2002), and plotted in Streckeisen (1976) classification diagram (not
224 shown). The normative contents of olivine, orthopyroxene, and clinopyroxene of the
225 studied Sol Hamed serpentinites classify them as harzburgites. Trace element values are
226 typical of residual mantle (e.g. high Cr (2.696–2.742 ppm), Ni (1.650–2.381 ppm) and Co
227 (116.20-166.79 ppm)). In contrast, the contents of Ba, Pb, Sr and, Li are highly
228 concentrated compare to depleted and pristine mantle peridotites (McDonough and Sun

229 1995). This enrichment in the fluid-mobile elements may be directly related to the
230 serpentinization process or due to metasomatism by subduction-related fluids (Hamdy et
231 al. 2013).

232

233

234 **6. Discussion**

235 *6.1. Origin and tectonic setting of the serpentinite protolith*

236 Earth contains two main shallow mantle domains: sub-oceanic lithosphere and sub-
237 continental lithosphere. The Sol Hamed harzburgite falls within the oceanic array (Niu
238 2004) in $\text{MgO}/\text{SiO}_2\text{--Al}_2\text{O}_3/\text{SiO}_2$ space (Fig. 5). The oceanic array is parallel to the
239 terrestrial array but offset to lower MgO/SiO_2 values, presumably due to loss of MgO
240 during low-temperature seafloor weathering and not due to the serpentinization process
241 itself (Snow and Dick 1995; Niu 2004). Oceanic peridotites may originate in a variety of
242 tectonic environments including mid-ocean ridge (MOR), suprasubduction zone (SSZ)
243 and rifted margins settings. We term these suprasubduction zone (SSZ) peridotites
244 (Pearce et al. 1984); a group that incorporates peridotites from both island arcs and
245 spreading centers above subduction zones. These discrete genetic types are distinct in
246 mineralogical and geochemical characteristics of mantle residues. Composition of the
247 unaltered accessory spinel is extensively used as a petrogenetic and geotectonic indicator
248 (e.g. Barnes and Roeder 2001). Chromium numbers $[\text{Cr}/(\text{Cr}+\text{Fe}^{3+}+\text{Al})]$ higher than 0.6
249 are usually restricted to subduction-related rocks (Dick and Bullen 1984). Ishii et al.
250 (1992) used the Mg# $[\text{Mg}/(\text{Mg}+\text{Fe}^{2+})]$ and Cr# of the spinel to discriminate between
251 peridotites from MOR, forearc and back-arc settings. Spinel from the Sol Hamed

252 serpentinites lie in the chemical space of the forearc peridotite (Fig.6) and distinctly
253 higher than spinels from MOR and back-arc basin in the Cr#. This indicates that the Sol
254 Hamed serpentinites represent a fragment of oceanic lithosphere that has been
255 incorporated above subduction zone in a forearc.

256 Hellebrand et al. (2001) tested which trace elements correlate with major element
257 indicators of partial melting in central Indian ridge peridotites. The most common of
258 these is the Cr# in spinel. They found a well-defined correlation between moderately
259 incompatible elements, such as HREEs in clinopyroxene with spinel Cr#. Hellebrand et
260 al. (2001) developed an empirical equation ($F = 10 \ln (\text{Cr\#}) + 24$) to estimate the degree
261 of melting F (in percent) as a function of spinel Cr#. Using the equation of Hellebrand et
262 al. (2001), the estimated melting in the studied peridotites ranges from 20 to 22%.

263

264 6.2. Thermodynamic modelling

265 All the thermodynamic calculations in the following sections were calculated by
266 THERMOCALC (Powell and Holland 1988), PerPle_X (Connolly 1990) and using the
267 internally consistent dataset of Holland and Powell (2011). Lizardite bearing reactions
268 which were proved experimentally (i.e. $\text{liz} = \text{br atg}$ (Evan 2004), $\text{liz} = \text{chr}$ (Chernosky
269 1975), $\text{liz} = \text{ta fo clin H}_2\text{O}$ (Caruso and Chernosky 1979)) will be only used (Fig. 7).

270 Figure 7 shows a P - T grid in the system CFMASH for the following end-members: atg,
271 chr, en, fs, di, hed, fo, fa, anth, tr, clin, ta, sp, herc, mgts, fta, br, H₂O. Activity of the H₂O
272 is imposed to be the unity therefore all the CO₂ bearing phases are not seen in this grid.
273 The P - T grid shows forty six univariant equilibria, five invariant points and three
274 experimental lizardite bearing reactions. All the H₂O bearing univariant reactions show

275 steep slope in the P - T space. Consequently these reactions can be used as temperature
276 indicators. Two water absent invariant points (508 °C-1.08 kbar and 542 °C-2.2 kbar)
277 involve reactions with notable change in the volume and can be used as pressure
278 indicators. For better reading to the P - T grid, only the interesting reactions are shown in
279 Figure 8 using two different scales for temperature axe.

280

281 *Anthophyllite and talc formation*

282 One of the key petrographic features is the relation between pyroxene, anthophyllite and
283 talc. The anthophyllite is a common replacement mineral of orthopyroxene. The
284 anthophyllite can be formed due to eight metamorphic reactions (Fig. 8), however the
285 absence of clinocllore and the formation of the talc psuedomorphic after anthophyllite
286 make the only possibility to crystallize anthophyllite is due to breakdown of high grade
287 minerals (i.e. pyroxene). Two reactions can produce anthophyllite during a retrograde
288 path at relatively high pressure (> 1.7 kbar) and above the atg-chr-fs-di-hed-fa-tr-ta-herc-
289 fta-br-mgts invariant point, however, these reactions produce clinocllore in considerable
290 values. This makes reaction fa anth=fs en H_2O and the lower pressure part (< 1.7 kbar) of
291 reaction fo anth=en H_2O are preferred way to produce anthophyllite in the assumed fluid
292 composition.

293 Eight reactions can produce talc as a retrograde phase due to breakdown of high grade
294 assemblage that includes anthophyllite. Four reactions can be excluded since they contain
295 clinocllore as a reactant or a product. The petrographic observation “orthopyroxene
296 consumed due to talc growing” makes fa ta=fs anth H_2O , ta sp= H_2O mgts anth reactions
297 (Fig. 8) are the favorable equilibria to produce talc. The two talc producing reactions

298 have a temperature range 630 - 790 °C in a wide pressure condition. The pressure
299 conditions of anthophyllite formation (< 1.7 kbar) make the upper temperature limit of
300 talc producing reactions is below 730 °C. Other reactions can produce anthophyllite and
301 talc in the same pressure-temperature range but with different fluid compositions, these
302 reactions will be discussed in the fluid composition section.

303 Talc and anthophyllite formations indicate isobaric cooling path at pressure below 1.7
304 kbar and in a temperature range of 800-550 °C. The cooling path can be extended to a
305 lower temperature condition based on the presence of lizardite in the studied assemblage.
306 This assumption is in agreement with the greenschist facies conditions of the intermediate
307 zone of the spinel grains (Fig. 4b).

308 Stern et al. (2004) reconstructed the ophiolitic sequence of the Arabian-Nubian Shield
309 and concluded that the ophiolitic successions have crustal thicknesses of 2.5 to 5 km.
310 These crustal thicknesses are equivalent to pressure 0.7 and 1.4 kbar, respectively (Fig. 8)
311 assuming lithostatic conditions and a rock density of $2.84 \times 10^3 \text{ kg/m}^3$ (Carlson and
312 Raskin 1984). This constrains pressure conditions of the formation of the anthophyllite
313 and talc process by 0.7-1.4 kbar (the retrograde path as shown by the black arrow in
314 Figure 8).

315

316 *Chrysotile formation and prograde metamorphism*

317 Presence of chrysotile fibers traversing the lizardite matrix indicates that the rocks passed
318 the reaction $\text{liz} = \text{chr}$ (Fig. 8). Hamdy and Lebda (2007) showed that the magnetite rims
319 of the chromite grains of Malo Grim serpentinites (part of the Sol Hamed ophiolites)
320 equilibrated at a temperature range of 500-550 °C. These conditions are in agreement

321 with the composition of the rim zones of the spinel grains which show condition of
322 amphibolite facies (Fig. 4b). Neither petrographic observations nor mineral chemistry
323 data allow predicting the pressure conditions of chrysotile formation.

324 The Arabian-Nubian shield ophiolites were obducted within volcanic arc assemblages
325 due to arc-arc collision process (e.g. Stern 1994; Kusky et al. 2003; Meert 2003; Stern et
326 al. 2004). Obducted ophiolites, associated volcanics and sediments may represent an
327 accretionary prism system. Here we will follow the assumption of Valli et al. (2004) that
328 average thermal gradient of ancient and modern accretionary prisms can be in the range
329 of 30 °C/km and 10 °C/km, respectively (Fig. 8). El-Naby and Frisch (1999) studied
330 Allaqi-Heiani ophiolite belt and they concluded that these ophiolites record temperature
331 of 700 °C and pressures up to 8 kbar. These conditions can be converted to a thermal
332 gradient of 25 °C/km which locates between the two assumed thermal gradient. This
333 thermal gradient cuts the predicted temperature (500-550 °C) in a pressure range of 5.5-
334 6.5 kbar (Fig. 8).

335

336 *Fluid composition and T-XCO₂ section*

337 Due to the ambiguity around the pressure condition during the prograde path of the
338 studied samples, the fluid composition will be studied only along the cooling path. Figure
339 9 shows a T-XCO₂ grid in the system CFMASH-CO₂ for the following end-members:
340 anth, atg, chr, en, fs, di, hed, fo, fa, ta, sp, herc, mgts, fta, mag, sid, H₂O, CO₂ at 1 kbar
341 (the cooling path of Figure 8). The T-XCO₂ grid was constructed in the full XCO₂ range
342 (not shown here), however all anthophyllite and talc producing invariant points occur at
343 high XCO₂ (> 0.88). In this type of sectioning (*P*-, *T*-XCO₂), mineral phases are produced

344 mainly at the invariant point conditions (Spear 1993). The grid includes twenty five
345 univariant reactions and seven invariant points. All of these invariant points occur at
346 temperature range of 450-520 °C (Fig. 9). All the invariant points above 500 °C are
347 magnesite-siderite absent invariant points. At 500 °C and X_{CO_2} (0.913), magnesite-
348 bearing invariant point appears. With cooling, the carbonate phase (siderite) becomes
349 more stable (at 460 °C and X_{CO_2} (0.978)). Below 450 °C, the magnesite becomes
350 metastable (Fig. 9). These invariant points show sequence of fluid evolution in the Sol
351 Hamed serpentinites.

352 At X_{CO_2} range (0.88-0.99), the first talc producing reaction ($ta\ sp=mgts\ anth\ H_2O$ (Fig.
353 9)) is at higher temperature than any anthophyllite producing reactions which were
354 discussed in the P - T grid. Consequently reaction ($herc\ anth=mgts\ en\ fs\ H_2O$) is the
355 preferred anthophyllite producing reaction. Once the rocks started the cooling path, the
356 anthophyllite producing reaction (op. cit.) buffers the fluid composition of the system and
357 the T - X_{CO_2} path (dashed arrows in Figure 9) followed the reaction till the mineral
358 composition arrives the $atg\ chr\ di\ hed\ fo\ fa\ sp\ fta\ mag\ sid\ CO_2$ invariant point (510 °C;
359 0.998 (X_{CO_2})). The assemblage stayed at the invariant point conditions until one of the
360 phases (i.e. fs , $herc$, $mgts$) was completely consumed or excluded out the equilibrium. At
361 this stage of the path, the rocks follow the isothermal reaction ($ta\ en=anth\ H_2O$) which
362 produces a considerable amount of talc. This reaction crosses all the invariant points at
363 510 °C with different X_{CO_2} composition (Fig. 9). Presence of magnesite in the studied
364 assemblage (Table 4) and presence of magnesite-bearing invariant point at 500 °C and
365 X_{CO_2} (0.913) make the only possibility to terminate the talc producing reaction (op. cit.)
366 is at the $atg\ chr\ fs\ di\ hed\ fa\ sp\ herc\ mgts\ fta\ mag\ sid\ CO_2$ invariant point (510 °C;

367 0.885 (X_{CO_2}). The assemblage stayed at this invariant point until the anthophyllite was
368 trapped and excluded out the equilibrium, afterward the mineral equilibrium follows the
369 reaction (fo ta=en H₂O) until the magnesite-bearing invariant point at 500 °C and X_{CO_2}
370 (0.913) which allows the first appearance of carbonate-bearing phase. Forsterite
371 consuming drives the equilibrium to leave the magnesite-bearing invariant point toward
372 the magnesite-siderite-bearing invariant point (460 °C and X_{CO_2} (0.978)). Subsequently
373 the reaction (ta sid=en fa CO₂ H₂O) buffers the equilibrium until the magnesite becomes
374 metastable at 450 °C and 0.984 (X_{CO_2}). Finally, reaction (ta sid=en fs CO₂ H₂O)
375 produces talc and siderite with constant consuming rate of H₂O and CO₂.

376

377 *6.3. Fluid source and Tectonic implications*

378 Decarbonation of altered metabasalts and carbonates of marine sediments at low pressure
379 condition has been considered as a possible mechanism in order to explain CO₂ fluxes at
380 convergent margins (Staudigel et al. 1996; Kerrick and Connolly 1998; Fischer et al.
381 1998; Molina and Poli 2000). When hot geotherms are assumed, CO₂-rich fluids can be
382 transferred from the altered oceanic crust to shallower reservoirs (Fig. 10) in the forearc
383 region (Molina and Poli 2000). This mechanism can account for the CO₂ enrichment of
384 lithospheric mantle on a long-term scale and it may explain the occurrence of carbonates
385 in peridotite xenoliths (Ionov et al. 1993) as well as in some camptonitic lamprophyres
386 (Bea et al. 1999). Here this mechanism can be used to explain the high CO₂ fluxes in the
387 studied ophiolites ($X_{CO_2} = 0.89-0.99$ (Fig. 9)). This high CO₂ fluid content reacted with
388 the ophiolitic rocks in the forearc (Fig. 10) under pressure condition of 1 kbar and
389 temperature of around 800 °C (Fig. 8). Stern and Gwinn (1990) argued on the basis of C

390 and Sr isotopic that carbonate intrusions in the Eastern Desert of Egypt - which could be
391 related to the carbonatizing fluids affecting Arabian-Nubian Shield ultramafic rocks - are
392 mixtures of mantle derived and remobilized sedimentary carbonate. Hamdy and Lebda
393 (2007) concluded the same conclusion based on carbon isotope composition of south
394 Eastern Desert of Egypt.

395 T - XCO_2 grid (Fig. 9) shows that the fluid composition was buffered all the time by the
396 metamorphic reactions (e.g. Greenwood 1975; Rice and Ferry 1982; Spear 1993; Abu-
397 Alam et al. 2010). Field, petrographical and mineral chemistry evidences support this
398 thermodynamic observation. Majority of the T - XCO_2 path took place at a temperature
399 range of 450 – 550 °C. Most of the reactions in this range of the temperature occurred as
400 isothermal reactions which means that the rocks were held at this temperature for a time
401 period enough to consume one phase or more to drive the equilibria toward a lower
402 temperature conditions. Figure 5a of Hamdy and Lebda (2007) shows that spinel minerals
403 of the studied ophiolites were re-equilibrated at temperature condition of 500-550 °C
404 which is the same range provided by the T - XCO_2 grid. Presence of magnesite in
405 considerable amount in thin-section scale as well as presence of small pockets and veins
406 of magnesite in outcrop scale, indicate that the rocks were held for a long time at the two
407 magnesite-bearing invariant points (at temperature 500 and 460 °C (Fig. 9)).

408 The high pressure condition (8 kbar) which was assumed by El-Naby and Frisch (1999)
409 and which was used here to predict the geothermal gradient and the prograde path (the
410 black arrow of Figure 8) as well the predicted pressure range (5.5-6.5 kbar from this
411 study) can be explained in the context of extensive duplex array and thickness of the
412 original ophiolitic sequence (e.g. Hirono and Ogawa 1998; Ueno et al. 2011). Oceanic

413 crust in a forearc setting can be overloaded by obduction of a crust that formed in a mid-
414 oceanic ridge and the thrusting in the forearc crust itself can add more loads (Fig. 10).
415 Original thickness of the Arabian-Nubian Shield's ophiolitic sequence is 2.5 to 5 km
416 (Stern et al. 2004). Following oceanic crust density of $2.84 \times 10^3 \text{ kg/m}^3$ (Carlson and
417 Raskin 1984), the studied ophiolites were overloaded by 20-28 km thickness of obducted
418 and thrusted oceanic crust from both mid-oceanic and forearc settings. This is in
419 agreement with thickness of the original sequence by a factor in range of 5.6 and 11.2.
420 The same thickening factors were suggested numerically by Ueno et al. (2011).
421 One of the opened questions around the ophiolites of the Arabian-Nubian Shield is "*when*
422 *did the alteration take place? Is it before or after the obduction?*" (Stern et al. 2004)".
423 Clearly, petrographic observations and thermodynamic modelling that are presented here
424 give an answer to this question. The studied ophiolites show two segments of the *P-T*
425 path; one is the isobaric cooling path at pressure condition of 1 kbar and the second is
426 prograde path from a pressure 1 kbar up to 5.5-6.5 kbar (black arrow of Figure 8). The
427 isobaric cooling path occurred under oceanic crustal thickness of 3.5 km which means
428 that the first stage of alteration took place before the obduction while the second stage
429 occurred during thrusting and obduction processes (prograde metamorphism). At today
430 situation, the ophiolites are thrusted over volcanic arc-assemblage. The volcanic arc-
431 assemblage of the Arabian-Nubian Shield records a peak pressure around 3-4 kbar (e.g.
432 Noweir et al. 2006; Abu-Alam 2005; Abu-Alam and Farahat unpublished data). This can
433 be ensued only if the ophiolites achieved the peak condition (5.5-6.5 kbar) before the
434 final thrusting above the low-pressure arc-assemblage.
435

436 **7. Conclusions**

437 The Sol Hamed serpentinitised ophiolitic mantle peridotite in the south Eastern Desert of
438 Egypt at the Allaqi-Heiani-Onib-Sol Hamed-Yanbu arc-arc suture formed in forearc
439 setting and later thrust over low-grade arc-assemblage of the Arabian-Nubian Shield. It
440 shows a *P-T* path of an isobaric cooling at lithostatic pressure of 1 kbar which is
441 equivalent to an oceanic crustal thickness of 3.5 km. The alteration occurred before the
442 thrusting and at high CO₂ fluxes. The decarbonation of altered oceanic metabasalts and
443 carbonates of marine sediments at low pressure condition can be considered as a possible
444 mechanism to explain the high concentrated CO₂ fluid fluxes at the convergent margin.
445 The concentration of the fluid during the cooling path was buffered by the metamorphic
446 reactions. The second segment of the path represents a prograde metamorphism which
447 occurred under extensive duplex array and thrusting of the oceanic crust. The crust in the
448 forearc basin was overloaded by 20-28 km of obducted and thrust oceanic crust from
449 both mid-oceanic and forearc basin. This is equivalent to thickness of the original
450 ophiolitic sequence by a factor in range of 5.6 and 11.2.

451

452 **Acknowledgements**

453 All analyses were carried out via personal communications. Sincere thanks are due to Dr.
454 Ryszard Orłowski and Mrs. Tatiana Wesolowska (Institute of Geological Sciences-Polish
455 Academy of Sciences) for help with the chemical analysis of minerals and whole rock,
456 respectively. We thank R. Stern and K. Stüwe for the discussion around accretionary
457 prisms. T. Holland is thanked for his help to provide a new thermodynamic dataset

458 includes lizardite. J. Connolly and F. Gallien are thanked for their help with PerPle-X
459 program. B. Evans is thanked for his help with inaccessible papers.

460

461 **References**

- 462 Abd El-Naby HH, Frisch W (2002) Origin of the Wadi Haimur-Abu Swayel gneiss belt,
463 south Eastern Desert, Egypt: Petrological and geochronological constraints.
464 Precamb Res 113:307–322.
- 465 Abd El-Rahman Y, Polat A, Dilek Y, Fryer BJ, El-Sharkawy M, Sakran S (2009)
466 Geochemistry and tectonic evolution of the Neoproterozoic incipient arc-forearc
467 crust in the Fawakhir area, Central Eastern Desert of Egypt. Precambrian Res
468 175:116–134.
- 469 Abdelsalam MG, Stern RJ (1993) Tectonic evolution of the Nakasib suture, Red Sea
470 Hills, Sudan: evidence for a late Precambrian Wilson Cycle. J Geol Soc 150:
471 393-404.
- 472 Abdelsalam MG, Stern RJ (1996) Sutures and shear zones in the Arabian-Nubian Shield.
473 J Afr Earth Sci 23: 289–310.
- 474 Abdelsalam MG, Abdeen MM, Dowaidar HM (2003) Structural evolution of the
475 Neoproterozoic Western Allaqi-Heiani suture, southeastern Egypt. Precambrian
476 Res 124: 87-104.
- 477 Abu-Alam TS (2005) Geological studies of the area around Wadi Kareim, Central
478 Eastern Desert, Egypt. M.Sc., Tanta University.
- 479 Abu-Alam TS, Santosh M, Brown M, Stüwe K (2013) Gondwana Collision. Miner Petrol
480 DOI 10.1007/s00710-013-0283-5
- 481 Abu-Alam TS, Stüwe K, Hauzenberger C (2010) Calc-silicates from Wadi Solaf region,
482 Sinai, Egypt. J Afr Earth Sci 58: 475–488.
- 483 Abu El Laban SA (2002) Some geological and geochemical studies in Abu Ramad Area,
484 South Eastern Desert, Egypt. PhD. Cairo University. p. 274.
- 485 Abzalov MZ (1998) Chrome-spinels in gabbro-wherlites intrusions of the Pechenga area,
486 Kola Peninsula, Russia: emphasis on the alteration features. Lithos 43: 109-134.

487 Ahmed AH, Arai S, Attia AK (2001) Petrological characteristics of podiform chromitites
488 and associated peridotites of Pan-African complexes of Egypt. *Mineralium*
489 *Depos* 36:72–84.

490 Ahmed AH, Hanghøj K, Kelemen PB, Hart SR, Arai S (2006) Osmium isotope
491 systematics of the Proterozoic and Phanerozoic ophiolitic chromitites: in situ ion
492 probe analysis of primary Os-rich PGM. *Earth Planet Sci Lett* 245:777–791.

493 Akaad MK, Abu El Ela AM (2002) Geology of the basement rocks in the eastern half of
494 the belt between latitudes 25° 30' and 26° 30'N Central Eastern Desert, Egypt.
495 Geological Survey of Egypt, Paper No. 78. 118p.

496 Ali KA, Azer MK, Gahlan HA, Wilde SA, Samuel MD, Stern RJ (2010) Age of
497 formation and emplacement of Neoproterozoic ophiolites and related rocks
498 along the Allaqi Suture, south Eastern Desert, Egypt. *Gond Res* 18:583–595.

499 Azer MK, Stern RJ (2007) Neoproterozoic (835-720 Ma) serpentinites in the Eastern
500 Desert, Egypt: Fragments of Fore-arc mantle. *J Geol* 15:457–472.

501 Azer MK, Samuel MD, Gahlan HA, Stern RJ, Ren M, Moussa HE (2013) Neoproterozoic
502 ophiolitic peridotites along the Allaqi-Heiani suture, South Eastern Desert,
503 Egypt. *Miner Petrol* DOI 10.1007/s00710-012-0204-z

504 Barnes SJ (2000) Chromite in komatiites, II. Modifications during greenschist to mid-
505 amphibolite facies metamorphism. *J. Petrol.*, 41: 387-409.

506 Barnes SJ, Roeder PL (2001) The Range of Spinel Compositions in Terrestrial Mafic and
507 Ultramafic Rocks. *J Petro* 42: 2279–2302.

508 Bea F, Monetero P, Molina JF (1999) Mafic precursors, peraluminous granitoids, and late
509 lamprophyres in the Avila batholith: a model for the generation of Variscan
510 batholiths in Iberia. *J Geol* 107: 399-419.

511 Bloomer SH, Taylor B, MacLeod CJ, Stern RJ, Fryer P, Hawkins JW, Johnson L (1995)
512 Early Arc Volcanism and the Ophiolite Problem: A Perspective from Drilling in
513 the Western Pacific. In: Taylor B, Natland J (Eds.) *Active Margins and Marginal*
514 *Basins of the Western Pacific*. American Geophysical Union, Washington, DC,
515 pp 1–30.

- 516 Carlson RL, Raskin GS (1984) Density of the ocean crust. *Nature* 311: 555-558.
- 517 Caruso LJ, Chernosky JV (1979) The stability of lizardite. *Can Mineral* 17: 757-769.
- 518 Chernosky JV (1975) Aggregate refractive indices and unit-cell parameters of synthetic
519 serpentine in the system MgO-Al₂O₂-SiO₂-H₂O. *Ameri Minera*. 60: 200-208.
- 520 Connolly JAD (1990) Multivariable phase-diagrams - an algorithm based on generalized
521 thermodynamics. *Amer J Sci* 290: 666-718.
- 522 Dalziel IWD (1997) Neoproterozoic-Paleozoic geography and tectonics: Review,
523 hypothesis, environmental speculation. *Geol Soc Ameri Bull* 109: 16-42.
- 524 Dick HJB, Bullen T (1984) Chromian spinel as a petrogenetic indicator in abyssal and
525 Alpine-type peridotites and spatially associated lavas. *Contrib Mineral Petrol*
526 86:54-76.
- 527 Dixon TH (1979) The evolution of continental crust in the Late Precambrian
528 Egyptian Shield. PhD Thesis, Univ California.
- 529 El-Gaby S (2005) Integrated evolution and rock classification of the Pan-African belt in
530 Egypt. First Symposium on the Classification of the Basement Complex of
531 Egypt, pp. 1-9.
- 532 El-Naby HA, FrischW, (1999) Metamorphic sole of Wadi Haimur-Abu Swayel ophiolite:
533 Implications on late Proterozoic accretion. In: Wall HD, Greiling RO (Eds.),
534 Aspects of Pan-African Tectonics. Heidelberg, Germany, pp 9-14.
- 535 El-Ramly MF, Greiling RO, Rashwan AA, Rasmy AH (1993) Explanatory note
536 to accompany the geological and structural maps of Wadi Hafafit area,
537 Eastern Desert of Egypt. *Geol Surv Egypt* 68: 1-53
- 538 Evans BW (2004) The serpentinite multisystem revisited: Chrysotile is metastable. *Inter*
539 *Geol Rev* 46:479-506.
- 540 Evans BW, Frost, BR (1975) Chrome-spinel in progressive metamorphism - a
541 preliminary analysis. *Geochim Cosmochim Acta* 39: 959-972.

- 542 Fischer TP, Giggenbach WF, Sano Y, Williams SN (1998) Fluxes and sources of
543 volatiles discharged from Kudryavy, a subduction zone volcano, Kurile Island.
544 Earth Planet Sci Lett 160: 81-96.
- 545 Fitches W, Graham R, Hussein I, Ries A, Shackleton R, Price R (1983) The late
546 Proterozoic ophiolite of Sol Hamed, NE Sudan. Precambrian Res 19:385-411.
- 547 Garson MS, Shalaby IM (1976) Precambrian-Lower Palaeozoic plate tectonics
548 and metagabbros in the Red Sea region. Spec Pap Geol Assoc Can 14:
549 573-596.
- 550 Gass IG (1977) The evolution of the Pan African crystalline basement in NE
551 Africa and Saudi Arabia. J Geol Soc Lond 134: 129-138.
- 552 Greenwood HJ (1975) Buffering of pore fluids by metamorphic reactions. Ameri J Sci
553 275: 573-593.
- 554 Greiling RO, Kröner A, El Ramly MF, Rashwan AA (1988) Structural relationships
555 between the southern and central parts of the Eastern Desert of Egypt: details of
556 a fold and thrust belt. In: El Gaby S, Greiling RO (eds) The Pan-African Belt of
557 Northeast Africa and adjacent areas. Vieweg and Sohn, Weisbaden, pp 121–145
- 558 Hamdy MM (2004) Continental upper mantle in the area of the Sudetes on the basis of
559 mineralogical and geochemical studies of ultramafic rock occurrences, SW
560 Poland. PhD Thesis, Institute of Geological Sciences, Polish Academy of
561 Sciences, 221p.
- 562 Hamdy MM (2007): Stable isotope and trace element characteristics of some
563 serpentinite-hosted vein magnesite deposits from the Eastern Desert of Egypt:
564 arguments for magmatism and metamorphism-related mineralising fluids.
565 M.E.R.C. Bulletin, 21, 29-50.
- 566 Hamdy MM, Lebda EM (2007) Metamorphism of ultramafic rocks at Gebel Arais and
567 Gebel Malo Grim, Eastern Desert, Egypt: mineralogical and O–H stable isotopic
568 constraints. Egypt J Geol 51: 105-124.

569 Hamdy MM, Lebda EM (2011) Al-compositional variation in ophiolitic chromitites from
570 the south Eastern Desert of Egypt: Petrogenetic implications. *J Geol Min Res* 3:
571 232-250.

572 Hamdy MM, Harraz HZ, Aly GA (2013) Pan-African (intraplate and subduction-
573 related?) metasomatism in the Fawakhir ophiolitic serpentinites, Central Eastern
574 Desert of Egypt: mineralogical and geochemical evidences. *Arab J Geosci*, 6,
575 13-33, DOI 10.1007/s12517-011-0319-2.

576 Hart SR, Zindler A (1986) In search of a bulk-Earth composition. *Chem Geol* 57: 247-
577 267.

578 Hellebrand E, Snow JE, Dick HJB, Hofmann AW (2001) Coupled major and trace elements as
579 indicators of the extent of melting in mid-ocean-ridge peridotites. *Nature* 410: 677–681.

580 Hirono T, Ogawa Y (1998): Duplex arrays and thickening of accretionary prisms: An example
581 from Boso Peninsula, Japan. *Geol* 26: 779-782.

582 Holland TJB, Powell R (2011) An improved and extended internally consistent thermodynamic
583 dataset for phases of petrological interest, involving a new equation of state for solids. *J*
584 *Meta Geol* 29: 333-383.

585 Hyndman RD, Peacock SM (2003) Serpentinization of the forearc mantle. *Earth Planet*
586 *Sci Lett* 212: 417-432.

587 Ionov DA, Dupuy C, O'Reilly SY, Kopylova MG, Genshaft YS (1993) Carbonated
588 peridotite xenoliths from Spitspergen: implications for trace element signature of
589 mantle carbonate metasomatism. *Earth Planet Sci Lett* 119: 283-297.

590 Ishii T, Robinson PT, Maekawa H, Fiske R (1992) Petrological studies of peridotites
591 from diapiric serpentinite seamounts in the Izu-Ogasawara-Mariana forearc. In:
592 Fryer P, Pearce JA, Stokking LB (eds.) *Proceedings of the Ocean Drilling*
593 *Program Scientific Results 125*. Ocean Drilling Program, College Station, TX,
594 pp 445–485.

595 Johnson PR, Kattan FH, Al-Saleh AM (2004) Neoproterozoic ophiolites in the Arabian
596 Shield. In: Kusky TM (ed) *Precambrian ophiolites and related rocks*. In:
597 *Developments in precambrian geology* 13, Elsevier, 129–162

598 Kerrick DM, Connolly JAD (1998) Subduction of ophicarbonates and recycling of CO₂
599 and H₂O. *Geology* 26: 375-378.

600 Kröner A, Greiling RO, Reischmann T, Hussein IM, Stern RJ, Durr S, Kruger J, Zimmer
601 M (1987) Pan-African crustal evolution in the Nubian segment of northeast
602 Africa. In: Kröner A (ed) Proterozoic lithospheric evolution. American
603 Geophysical Union, Geodynamics Series 17: 237-257.

604 Kusky TM, Ramadan TM (2002) Structural controls on Neoproterozoic mineralization in
605 the South Eastern Desert, Egypt: an integrated field, Landsat TM, and SIR-C/X
606 SAR approach. *J Afr Earth Sci* 35:107–121

607 Kusky TM, Abdelsalam M, Tucker R, Stern R (2003) Evolution of the East African and
608 Related Orogens, and the Assembly of Gondwana. Special Issue of Precambrian
609 Res 123: 81–344.

610 Lebda, E.M., 1995, Petrology and mineral chemistry of serpentinite rocks of the
611 Gogołów-Jordanów massif, SW Poland. Ph.D. Thesis, Wrocław University,
612 Poland, 189p.

613 Li Z-X A, Lee C-T A (2006) Geochemical investigation of serpentinitized oceanic
614 lithospheric mantle in the Feather River Ophiolite, California: Implications for
615 the recycling rate of water by subduction. *Chem Geol* 235: 161-185.

616 McDonough WF, Sun SS (1995) Composition of the Earth. *Chem Geol* 120: 223-253.

617 Meert, JG (2003) A synopsis of events related to the assembly of eastern Gondwana.
618 *Tectonophy* 362, 1–40.

619 Melcher F, Meisel T, Puhl J, Koller F (2002) Petrogenesis and geotectonic setting of
620 ultramafic rocks in the Eastern Alps: constraints from geochemistry. *Lithos* 65:
621 69-112.

622 Molina JF, Poli S (2000) Carbonate stability and fluid composition in subducted oceanic
623 crust: an experimental study on H₂O-CO₂-bearing basalts. *Earth Planet Sci*
624 *Lett* 176: 295-310.

- 625 Niu YL (2004) Bulk-rock major and trace element compositions of abyssal peridotites:
626 Implications for mantle melting, melt extraction and post-melting processes
627 beneath ocean ridges. *J Petro* 45: 2423-2458.
- 628 Noweir MA, Ghoneim MF, Abu-Alam TS (2006) Deformational phases and tectonic
629 evolution of the Neoproterozoic rocks of Wadi Kareim area, Central Eastern
630 Desert, Egypt. *Annals J. Geol. Surv.*, 28, 81-109.
- 631 Patchett PJ, Chase CG (2002) Role of transform continental margins in major crustal
632 growth episodes. *Geology* 30: 39–42.
- 633 Pearce JA, Lippard SJ, Roberts S (1984) Characteristics and tectonic significance of
634 suprasubduction zone ophiolites. In: Kokelaar BP, Howell MF (Eds) *Marginal
635 Basin Geology*. Geological Society of London, pp. 77–94.
- 636 Powell R, Holland TJB (1988) An internally consistent thermodynamic dataset with
637 uncertainties and correlations: 3. Application, methods, work examples and a
638 computer program. *J Meta Geol* 6: 173-204.
- 639 Proenza JA, Ortega-Gutiérrez F, Camprubí A, Tritlla J, Elías-Herrera M, Reyes-Salas M
640 (2004) Paleozoic serpentinite-enclosed chromitites from Tehuizingo (Acatlán
641 Complex, southern Mexico): a petrological and mineralogical study. *J. S. Am.
642 Earth Sci.*, 16: 649-666.
- 643 Purvis AC, Nesbitt RW, Halberg JA (1972) The geology of part of Carr Boyd Complex
644 and its associated nickel mineralization, Western Australia. *Econ Geol* 67:
645 1093-1113.
- 646 Rice JM, Ferry JM (1982) Buffering, infiltration and the control of intensive variables
647 during metamorphism. In: Ferry JM, *Characterization of Metamorphism through
648 Mineral Equilibria*. Reviews in Mineralogy, 10, Mineralogical Society of
649 America, Washington, D. C. pp 263-326.
- 650 Snow JE, Dick HJB (1995) Pervasive Magnesium Loss by Marine Weathering of
651 Peridotite. *Geochim. Cosmochim. Acta* 59: 4219-4235.
- 652 Spear FS (1993) *Metamorphic phase equilibria and pressure-temperature-time paths*.
653 Mineralogical Society of America, USA.

- 654 Staudigel H, Plank T, White B, Schmincke HU (1996) Geochemical fluxes during
655 seafloor alteration of the basaltic upper oceanic crust DSDP Site 417 and 418,
656 AGU Geo phys Monogr 96: 19-37.
- 657 Stern R (1994) Arc assembly and continental collision in the neoproterozoic east African
658 orogen: implications for the consolidation of Gondwana. *Ann Rev Earth Planet*
659 *Sci Lett* 152:75–91.
- 660 Stern RJ, Gwinn CJ (1990) Origin of late precambrian intrusive carbonates, Eastern
661 Desert of Egypt and Sudan: C, O and Sr isotopic evidences. *Precam Res* 46:259–
662 272.
- 663 Stern R, Johnson PR, Kröner A, Yibas B (2004) Neoproterozoic ophiolites of the
664 Arabian–Nubian Shield. In: Kusky TM (ed) *Precambrian ophiolites and related*
665 *rocks. Developments in Precambrian geology, vol 13. Elsevier, Amsterdam, pp*
666 *95–128.*
- 667 Stern R, Nielsen K, Best E, Sultan M, Arvidson R, Kröner A (1990) Orientation of late
668 Precambrian sutures in the Arabian-Nubian shield. *Geology* 18: 1103–1106.
- 669 Stevens, R. E., 1944, Composition of some chromites of the Western Hemisphere. *Ameri*
670 *Minera.* 29, 1-34.
- 671 Streckeisen A (1976) Classification of the common igneous rocks by means of their
672 chemical composition. A provisional attempt. *Neues Jahr Buch für Mineralogie,*
673 *1: 1-15.*
- 674 Suita MTF, Strieder AJ (1996) Cr-spinel from Brazilian mafic-ultramafic complexes:
675 metamorphic modifications. *Int Geol Rev* 38: 245-267.
- 676 Taylor WEG, El Kazzaz YAH, Rashwan AA (1993) An outline of the tectonic
677 framework for the Pan-African orogeny in the vicinity of Wadi Um Relan area,
678 south Eastern Desert, Egypt. In: Thorweile U, Schandeimeier H (eds)
679 *Geoscientific research in northeast Africa, 31–34*
- 680 Ueno H, Hisada KI, Ogawa Y (2011) Numerical estimation of duplex thickening in a
681 deep-level accretionary prism: A proposal for network duplex. *GSA Special*
682 *Papers* 480, 207-213.

- 683 Vail JR (1983) Pan-African crustal accretion in north-east Africa. *J Afr Earth Sci* 1: 285-
684 294.
- 685 Valli F, Guillot S, Hattori KH (2004) Source and tectono-metamorphic evolution of
686 mafic and pelitic metasedimentary belt, Archean Superior Province of Canada.
687 *Precambrian Res* 132: 155-177.
- 688 Workman, R.K. and Hart, S.R. (2005). Major and trace element composition of the
689 depleted MORB mantle (DMM). *Earth Planet Sci Lett* 231: 53-72.
- 690 Zoheir BA, Klemm DD (2007) The tectono-metamorphic evolution of the central part of
691 the Neoproterozoic Allaqi-Heiani suture, south Eastern Desert of Egypt. *Gond*
692 *Res* 12:289–304.
- 693

694 **List of Figs.**

695 **Fig. 1.** Distribution of the ophiolites in the Arabian-Nubian Shield (modified after Vail
696 1983; Abu-Alam et al. unpublished data).

697 **Fig. 2.** Geological map of Sol Hamed area modified after Abu El-Laban 2002.

698 **Fig. 3.** (a) Semi-schematic drawing showing the ophiolitic ultramafic of Sol Hamed area,
699 lizardite and anthophyllite are metamorphosed after orthopyroxene. Chrysotile is
700 metamorphosed after lizardite. Talc is after anthophyllite. Liz, opx, anth, mag
701 and s are lizardite, orthopyroxene, anthophyllite, magnesite and sulphites,
702 respectively. (b) Zoned spinel in Sol Hamed serpentinite. Darker zones are
703 richer in Cr.

704 **Fig. 4.** Mineral chemistry. a) Substitution in serpentine. Aluminum and chromium are
705 grouped together, as they tend to vary sympathetically. b) Compositional
706 changes in spinels expressed in a triangular Cr-Fe³⁺-Al³⁺ plot with reference to
707 the fields of spinel types: a-aluminian chromite, b-ferrian chromite, c-chromian
708 magnetit, d-aluminian magnetite, e-ferrian spinel and f-chromian spinel (Stevens
709 1944) and the different metamorphic facies defined by Purvis et al. (1972);
710 Evans and Frost (1975) and Suita and Streider (1996).

711 **Fig. 5.** Whole rock MgO/SiO₂-Al₂O₃/SiO₂ plot. The terrestrial array is a compilation of
712 subcontinental peridotites (Hart and Zindler 1986) and represents a melt
713 depletion trend. The Sol Hamed serpentinites plot offset to lower MgO/SiO₂
714 values because of alteration. Compositions of depleted MORB mantle (DMM;

715 Workman and Hart 2005), primitive mantle (PM; McDonough and Sun 1995)
716 and seafloor weathering trend (Snow and Dick 1995) are plotted for comparison.

717 **Fig. 6.** Composition of spinels compared with those in modern peridotites. Data are
718 plotted on 100Cr/Cr+Al (Cr#) vs. 100Mg/Mg+Fe (Mg#) diagram, modified after
719 Dick and Bullen (1984). The fields are after Bloomer et al. (1995).

720 **Fig. 7.** *P-T* grid in the system CFMASH for atg, chr, en, fs, di, hed, fo, fa, anth, tr, clin,
721 ta, sp, herc, mgts, fta, br, H₂O. Activity of the H₂O is imposed to be the unity.
722 Note: reactions liz = br atg, liz = chr, liz = ta fo clin H₂O are used here after
723 Evan 2004; Chernosky 1975; Caruso and Chernosky 1979, respectively.

724 **Fig. 8.** A simplified *P-T* grid of Figure 7 shows only the interesting metamorphic
725 reactions. Maximum pressure during the cooling path is the pressure equivalent
726 to the invariant point [atg chr fs di hed fa tr ta herc fta br mgts]. The vertical bar
727 below the op. cit. invariant point shows the pressure equivalents to the Arabian-
728 Nubian Shield's ophiolitic crustal thicknesses as reconstructed by Stern et al.
729 (2004). The two gray arrows show the modern thermal gradient and ancient
730 thermal gradient. The black arrow showing the path of the study samples, the
731 peak pressure is 5-5.7 kbar based on the pressure calculation from Wadi
732 Haimur-Abu Swayel ophiolites (El-Naby and Frisch 1999). Note: the ancient
733 thermal gradient is equivalent to thickening of the sequence by factor of 5.5 as
734 suggest by Ueno et al. (2011). The temperature axe is in two different scales to
735 show the reactions at high temperature condition in more details than Figure 7.

736 **Fig. 9.** A *T-XCO₂* grid in the system CFMASH-CO₂ for the following end-members:
737 anth, atg, chr, en, fs, di, hed, fo, fa, ta, sp, herc, mgts, fta, mag, sid, H₂O, CO₂.

738 The grid was constructed at 1 kbar. Fluid concentration is buffered by the
739 metamorphic reactions. The grid shows high CO₂ concentration in the fluid

740 **Fig. 10.** A three dimensional model illustrating the tectonic evolution of the studied
741 ophiolites. a) Development of subduction zone. High concentrated CO₂ fluid is
742 released from carbonate rocks in the subduction zone. These fluids re-
743 concentrated in the fore-arc ophiolites. A passive margin is drawn on the flank
744 of the oceanic basin since some authors recorded volcanic and sedimentary
745 rocks in the Arabian-Nubian Shield were formed in a passive margin setting
746 (e.g. Nakasib suture; Abdelsalam and Stern 1993). b) Thrusting and duplex
747 thickening of the ophiolitic sequence. The white star is the position of the
748 studied ophiolites.

749

750 **List of Tables**

751 **Table 1.** Summary of mineral assemblages of the studied ultramafic rocks.

752 **Table 2.** Orthopyroxene and serpentine analyses.

753 **Table 3.** Talc analyses. The chemical formula was calculated based on 11 oxygen atoms
754 and ignoring the H₂O.

755 **Table 4.** Carbonate analyses. The chemical formula was calculated based on 2 cations.

756 **Table 5.** Spinel group analyses. The chemical formula was calculated based on 24
757 oxygen atoms. b.d.l is below detection limit.

758 **Table 6.** Representative whole-rock chemistry of Sol Hamed serpentinites. Major oxides
759 are in wt%, trace elements are in ppm. b.d.l is below detection limit.

Primary minerals	Olivine Opx Spinel Chromite (the inner core)
First stage of alteration and metamorphism	Lizardite Antigorite Anthophyllite Magnesite Magnetite Chromite (inter. zone) Sulphides
Second stage of alteration and metamorphism	Lizardite Chrysotile Talc Magnesite Magnetite Chromite (outer zone)

Table 1

Abu-Alam and Hamdy (2013)

Fluid interaction in the Arabian-Nubian Shield ophiolites

Table

[Click here to download Table: Table 2.doc](#)

Sample	Opx		Serpentine														
	325/1	325/2	323	324	324	324	325	325	333	333	278	278	310	347	347	369	369
SiO ₂	58.21	58.37	43.73	41.86	42.62	41.13	42.47	42.6	40.62	43.78	44.54	43.04	43.96	41.56	41.3	43.23	41.94
TiO ₂	0.12	0.09	0.12	b.d.1	0.01	0.03	b.d.1	0.01	0.12	0.08	0.07	0.15	0.08	0.01	b.d.1	b.d.1	0.03
Al ₂ O ₃	0.74	0.67	0.48	0.46	1.12	1.79	0.13	b.d.1	0.3	0.06	0.28	0.14	0.14	0.14	0.26	0.21	0.28
Cr ₂ O ₃	0.42	0.36	b.d.1	b.d.1	0.16	0.02	0.02	b.d.1	0.22	b.d.1	b.d.1	0.34	0.12	0.09	0.16	0.15	0.36
FeO	4.85	5.09	2.61	2.88	1.98	3.33	1.81	2.05	4.2	2.66	1.37	1.85	0.94	3.99	3.36	2.11	6.21
MnO	0.03	0.07	0.09	b.d.1	0.04	b.d.1	b.d.1	b.d.1	0.38	b.d.1	0.01	0.09	b.d.1	0.17	0.22	0.01	b.d.1
MgO	34.99	35.1	37.04	37.04	37.67	36.99	38.42	36.68	34.37	37.74	37.78	36.88	38.14	38.06	38.68	37.17	35.98
CaO	b.d.1	0.03	b.d.1	0.1	b.d.1	b.d.1	b.d.1	0.19	0.03	0.07	0.06	0.13	b.d.1	b.d.1	b.d.1	0.18	0.11
Na ₂ O	b.d.1	b.d.1	0.13	0.01	0.05	0.05	0.02	b.d.1	b.d.1	0.12	0.01	0.01	0.1	b.d.1	b.d.1	0.09	0.08
K ₂ O	b.d.1	b.d.1	b.d.1	0.02	0.03	b.d.1	0.01	0.03	b.d.1	0.01	0.02	0.03	0.08	0.01	b.d.1	0.08	0.01
Total	99.36	99.78	84.2	82.37	83.68	83.34	82.88	81.56	80.24	84.52	84.14	82.66	83.56	84.03	83.98	83.23	85
Si	2	2	8.381	8.237	8.211	8.027	8.258	8.41	8.283	8.369	8.47	8.385	8.418	8.097	8.036	8.375	8.162
Ti	0.003	0.002	0.017	-	0.001	0.004	-	0.001	0.018	0.012	0.01	0.022	0.012	0.001	-	-	0.004
Al	0.03	0.027	0.108	0.107	0.254	0.411	0.03	-	0.072	0.014	0.063	0.032	0.032	0.032	0.06	0.048	0.064
Cr	0.011	0.01	-	-	0.024	0.003	0.003	-	0.035	-	-	0.052	0.018	0.014	0.025	0.023	0.055
Fe	0.139	0.146	0.418	0.474	0.319	0.543	0.294	0.338	0.716	0.425	0.218	0.301	0.151	0.65	0.547	0.342	1.011
Mn	0.001	0.002	0.015	-	0.007	-	-	-	0.066	-	0.002	0.015	-	0.028	0.036	0.002	-
Mg	1.792	1.792	10.58	10.86	10.82	10.76	11.13	10.79	10.44	10.75	10.71	10.71	10.88	11.05	11.21	10.73	10.43
Ca	-	0.001	-	0.021	-	-	-	0.04	0.007	0.014	0.012	0.027	-	-	-	0.037	0.023
Na	-	-	0.048	0.004	0.019	0.019	0.008	-	-	0.044	0.004	0.004	0.037	-	-	0.034	0.03
K	-	-	-	0.005	0.007	-	0.002	0.008	-	0.002	0.005	0.007	0.02	0.002	-	0.02	0.002
Cations	3.977	3.98	19.57	19.71	19.66	19.77	19.73	19.59	19.65	19.64	19.49	19.56	19.58	19.88	19.92	19.62	19.79
en	0.93	0.92															
fs	0.0055	0.006															
mgts	0.027	0.01															

Table 2
Abu-Alam and Hamdy (2013)
Fluid interaction in the Arabian-Nubian Shield ophiolites

Table

[Click here to download Table: Table 3.doc](#)

Sample	Talc								
	306/2	306/2	306/2	306/2	306/2	347/2	347/2	347/2	347/2
SiO ₂	61.07	60.04	60.92	59.98	61.09	56.78	57.36	57.22	57.21
TiO ₂	0.05	b.d.1	0.04	0.07	0.22	b.d.1	b.d.1	b.d.1	b.d.1
Al ₂ O ₃	0.03	0.14	0.28	0.05	b.d.1	0.42	0.5	0.37	0.34
Cr ₂ O ₃	0.02	0.14	0.26	0.03	b.d.1	0.28	0.2	0.21	0.17
Fe ₂ O ₃	b.d.1	b.d.1	b.d.1	b.d.1	b.d.1	0.68	0.64	0.64	0.62
FeO	3.31	3.61	3.85	2.71	3.11	5.54	5.22	5.16	5.04
MnO	b.d.1	b.d.1	0.04	b.d.1	b.d.1	b.d.1	0.16	b.d.1	0.2
MgO	27.14	26.91	26.85	27.17	27.6	34.4	34.26	34.41	34.84
CaO	0.09	0.02	b.d.1	0.15	0.16	b.d.1	b.d.1	b.d.1	b.d.1
Na ₂ O	0.13	b.d.1	0.16	0.17	0.13	b.d.1	b.d.1	b.d.1	b.d.1
Totals	91.84	90.86	92.4	90.33	92.31	98.1	98.34	98	98.42
Si	4.053	4.036	4.034	4.041	4.035	3.646	3.666	3.667	3.654
Ti	0.002	-	0.002	0.004	0.011	-	-	-	-
Al	0.002	0.011	0.022	0.004	-	0.032	0.038	0.028	0.026
Cr	0.001	0.007	0.014	0.002	-	0.014	0.01	0.011	0.009
Fe ³⁺	-	-	-	-	-	0.033	0.031	0.031	0.03
Fe ²⁺	0.184	0.203	0.213	0.153	0.172	0.297	0.279	0.276	0.269
Mn	-	-	0.002	-	-	-	0.009	-	0.011
Mg	2.685	2.696	2.65	2.728	2.717	3.292	3.263	3.286	3.316
Ca	0.006	0.001	-	0.011	0.011	-	-	-	-
Na	0.017	-	0.021	0.022	0.017	-	-	-	-
Sum	6.951	6.955	6.957	6.964	6.962	7.316	7.296	7.3	7.315
ta	0.71	0.72	0.68	0.75	0.74	0.83	0.83	0.85	0.85
fta	0.00023	0.00031	0.00036	0.00013	0.00019	0.00061	0.00052	0.00051	0.00046

Table 3
 Abu-Alam and Hamdy (2013)
 Fluid interaction in the Arabian-Nubian Shield ophiolites

Table

[Click here to download Table: Table 4.doc](#)

Carbonate minerals													
Sample	300	300	300	306	306	306	306	306	306	368	368	368	368
SiO ₂	0.19	0.15	0.04	0.11	0.23	0.18	0.05	0.04	0.09	0.13	0.16	0.1	0.09
Cr ₂ O ₃	0.11	0.04	0.09	b.d.1	0.07	b.d.1	b.d.1	b.d.1	b.d.1	0.05	0.04	0.02	0.07
FeO	13.47	11.17	13.42	14.1	12.33	8.46	13.03	13.08	13.79	8.97	13.06	13.95	10.63
MnO	0.09	0.25	0.13	0.33	0.33	0.22	0.03	0.08	0.17	0.24	0.25	0.25	0.27
MgO	36.19	38.06	36.82	35.53	36.53	40.14	36.57	36.09	36.63	39.53	36.58	36.08	38.07
CaO	0.11	0.23	0.17	0.15	0.15	0.24	0.04	0.21	0.27	0.17	0.21	0.21	0.15
Totals	50.16	49.9	50.67	50.22	49.64	49.24	49.72	49.5	50.95	49.09	50.3	50.61	49.28
Si	0.006	0.004	0.001	0.003	0.007	0.005	0.002	0.001	0.003	0.004	0.005	0.003	0.003
Cr	0.003	0.001	0.002	-	0.002	-	-	-	-	0.001	0.001	0	0.002
Fe ²⁺	0.343	0.28	0.338	0.361	0.315	0.21	0.333	0.336	0.346	0.224	0.331	0.354	0.269
Mn	0.002	0.006	0.003	0.009	0.009	0.006	0.001	0.002	0.004	0.006	0.006	0.006	0.007
Mg	1.643	1.701	1.65	1.622	1.663	1.772	1.664	1.653	1.638	1.759	1.65	1.63	1.715
Ca	0.004	0.007	0.005	0.005	0.005	0.008	0.001	0.007	0.009	0.005	0.007	0.007	0.005
Sum	2	2	2	2	2	2	2	2	2	2	2	2	2
mag	0.84	0.86	0.84	0.83	0.84	0.89	0.85	0.84	0.83	0.89	0.84	0.83	0.87
sid	0.26	0.21	0.25	0.27	0.24	0.17	0.25	0.25	0.26	0.18	0.25	0.26	0.21

Table 4

Abu-Alam and Hamdy (2013)

Fluid interaction in the Arabian-Nubian Shield ophiolites

Table

[Click here to download Table: Table 5.doc](#)

	Spinel																
	core02	rim03	core05	rim06	rim	core	core-rim	rim	core	core-rim	rim	core	core-rim	rim	core	core-rim	rim
SiO ₂	0,07	0,05	0,07	0,23	0,13	0,24	b.d.1	0,21	0,05	0,02	0,22	0,19	0,12	0,21	0,22	0,04	0,35
TiO ₂	0,36	0,23	0,21	0,18	b.d.1	0,22	0,27	b.d.1	0,15	b.d.1	0,02	0,21	0,13	b.d.1	0,08	0,11	b.d.1
Al ₂ O ₃	8,81	9,23	8,28	8,4	b.d.1	6,27	6,32	0,12	5,4	6,53	0,1	6,67	6,5	b.d.1	5,57	6,49	0,15
FeO	34,12	34,47	31,23	32,51	89,78	32,88	31,47	90,89	34,12	32,71	91,34	31,6	32,14	90,03	30,39	30,7	90,16
Cr ₂ O ₃	51,38	51,1	53,76	52,76	1,64	56,51	56,62	1,56	56,25	55,26	1,34	55,82	55	2,1	56,98	56,84	0,75
MnO	0,39	b.d.1	0,36	0,51	0,46	0,18	0,92	0,5	0,02	0,54	0,41	0,66	1,09	0,45	0,85	0,25	0,11
MgO	4,23	4,03	4,96	4,56	1	4,03	4,52	0,88	3,67	4,4	1,05	4,07	4,06	0,75	4,53	5,17	1,03
NiO	b.d.1	0,72	0,48	0,17	0,35	b.d.1	0,22	0,72	0,01	b.d.1	0,23	0,02	0,25	0,38	0,34	b.d.1	0,46
Total	99,36	99,83	99,35	99,32	93,36	100,33	100,34	94,88	99,67	99,46	94,71	99,24	99,29	93,92	98,96	99,6	93,01
Si	0,02	0,014	0,02	0,065	0,052	0,068	-	0,083	0,014	0,006	0,087	0,054	0,035	0,084	0,063	0,011	0,141
Al	2,96	3,084	2,76	2,809	-	2,099	2,113	0,056	1,84	2,207	0,047	2,249	2,203	-	1,889	2,17	0,071
Ti	0,08	0,049	0,045	0,038	-	0,047	0,058	-	0,033	-	0,006	0,045	0,028	-	0,017	0,023	-
Cr	11,56	11,451	12,018	11,83	0,522	12,687	12,692	0,488	12,852	12,526	0,42	12,623	12,499	0,663	12,956	12,744	0,239
Mn	0,094	-	0,086	0,123	0,157	0,043	0,221	0,168	0,005	0,131	0,138	0,16	0,266	0,152	0,207	0,06	0,038
Mg	1,796	1,705	2,093	1,93	0,6	1,708	1,913	0,52	1,583	1,883	0,621	1,737	1,742	0,447	1,944	2,188	0,62
Ni	-	0,16	0,11	0,04	0,11	-	0,05	0,23	-	-	0,07	-	0,06	0,12	0,08	-	0,15
Fe ²⁺	6,11	6,135	5,711	5,907	7,133	6,249	5,816	7,082	6,412	5,986	7,171	6,103	5,932	7,281	5,769	5,752	7,192
Fe ³⁺	1,39	1,402	1,157	1,258	15,426	1,099	1,137	15,373	1,261	1,261	15,44	1,029	1,235	15,253	1,075	1,052	15,549
Mg#	0,227	0,217	0,268	0,246	0,079	0,214	0,247	0,068	0,197	0,239	0,079	0,221	0,227	0,057	0,252	0,275	0,079
Cr#	0,726	0,718	0,754	0,744	0,0321	0,798	0,796	0,030	0,805	0,783	0,026	0,793	0,784	0,041	0,813	0,798	0,015
Fe ³⁺ #	0,087	0,087	0,072	0,079	0,967	0,069	0,071	0,965	0,079	0,078	0,970	0,064	0,077	0,958	0,067	0,065	0,980
mt	0,004	0,006	0,005	0,004	0,90	0,0013	0,0015	0,90	-	0,0009	0,89	0,0026	0,0012	0,90	0,0008	0,0018	0,91
cmt	0,39	0,39	0,41	0,40	0,00058	0,48	0,46	0,00052	0,50	0,45	0,0004	0,47	0,46	0,001	0,48	0,45	0,0001

Table 5

Abu-Alam and Hamdy (2013)

Fluid interaction in the Arabian-Nubian Shield ophiolites

Table[Click here to download Table: Table 6.doc](#)

Oxide	306	347	369	310
TiO ₂	0.06	0.02	0.01	0.04
SiO ₂	41.49	38.41	38.55	38.00
Al ₂ O ₃	0.48	0.31	0.80	0.88
Fe ₂ O ₃	6.79	7.54	8.70	7.49
MnO	0.09	0.09	0.09	0.07
MgO	38.99	38.43	39.83	39.11
CaO	0.18	1.19	0.65	0.12
Na ₂ O	0.09	b.d.1	0.01	0.17
K ₂ O	0.01	b.d.1	0.01	0.05
Sum	88.19	86.00	88.65	85.94
LOI	10.60	12.99	10.27	13.14
Cr	2742.20	2717.47	2703.71	2696.98
Co	166.79	154.23	116.20	120.41
Ni	2381.21	2060.51	1650.08	1799.16
Cu	63.83	8.27	46.32	14.97
Zn	57.11	16.55	11.98	13.32
Sr	55.04	89.11	48.08	46.61
V	40.31	14.00	33.93	29.83
Ba	35.24	45.00	20.00	15.00
Pb	4.70	4.63	24.04	13.15
Cd	2.00	3.31	3.43	2.00
Li	10.08	9.93	1.68	4.99
Rb	1.80	0.86	0.17	0.97

Table 6
Abu-Alam and Hamdy (2013)
Fluid interaction in the Arabian-Nubian Shield ophiolites

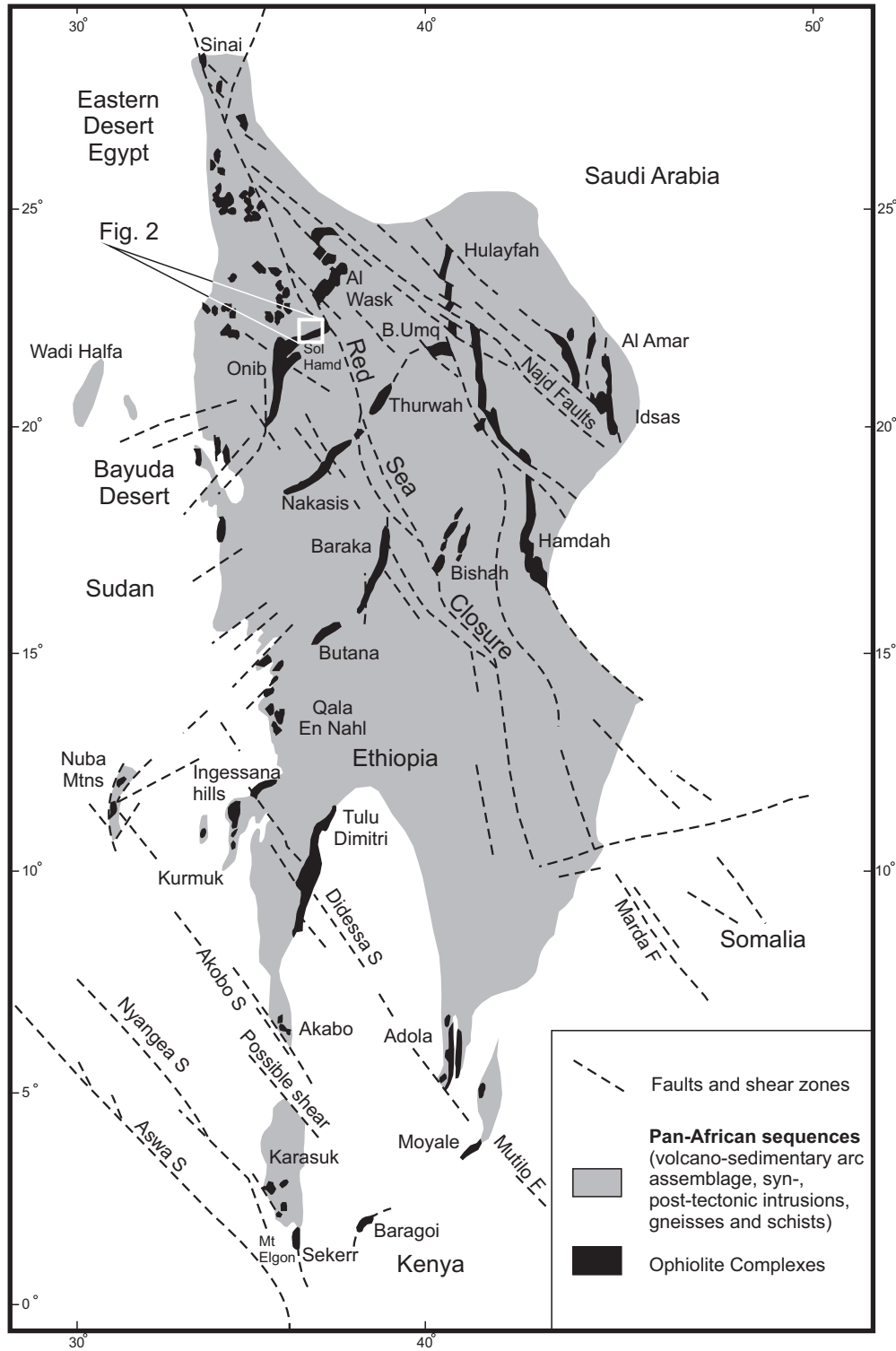


Fig. 1
Abu-Alam and Hamdy (2013)

Fluid interaction in the Arabian-Nubian Shield ophiolites

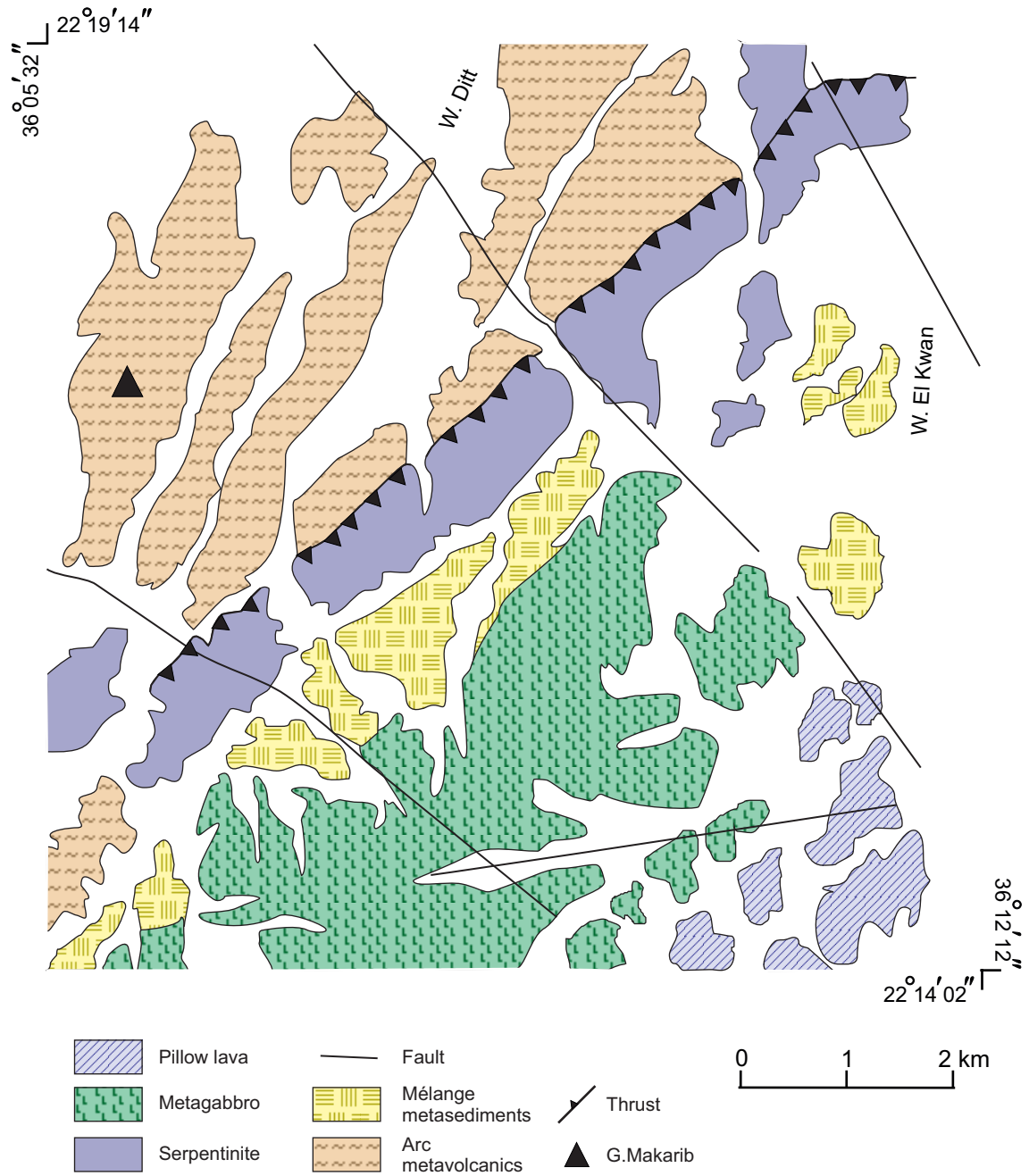
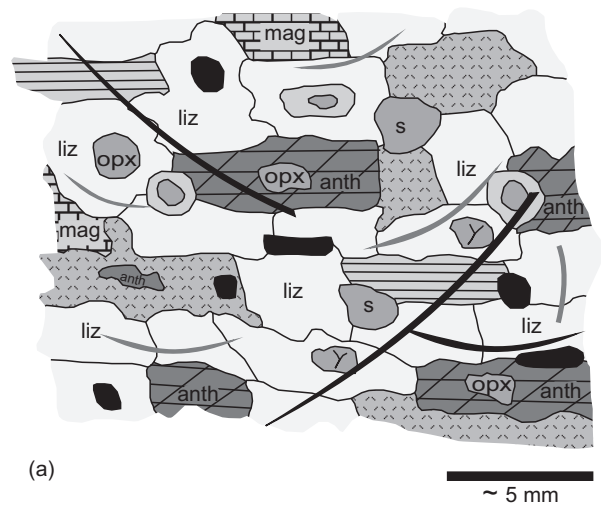
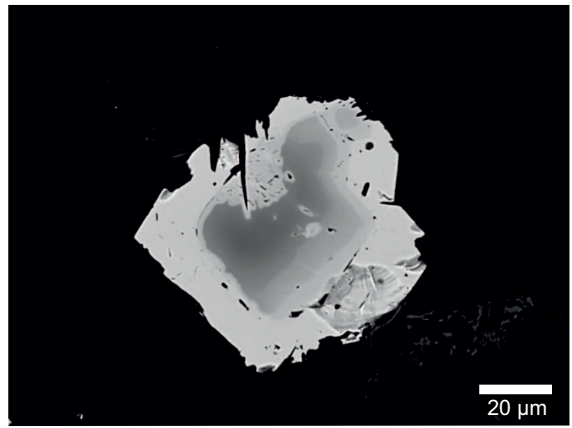


Fig. 2
Abu-Alam and Hamdy (2013)

Fluid interaction in the Arabian-Nubian Shield ophiolites



(a)



(b)







-  Chrysotile
-  Chlorite
-  Olivine
-  Talc
-  Zoned Chromite
-  Magnetite and spinel

Fig. 3
Abu-Alam and Hamdy (2013)
Fluid interaction in the Arabian-Nubian Shield ophiolites

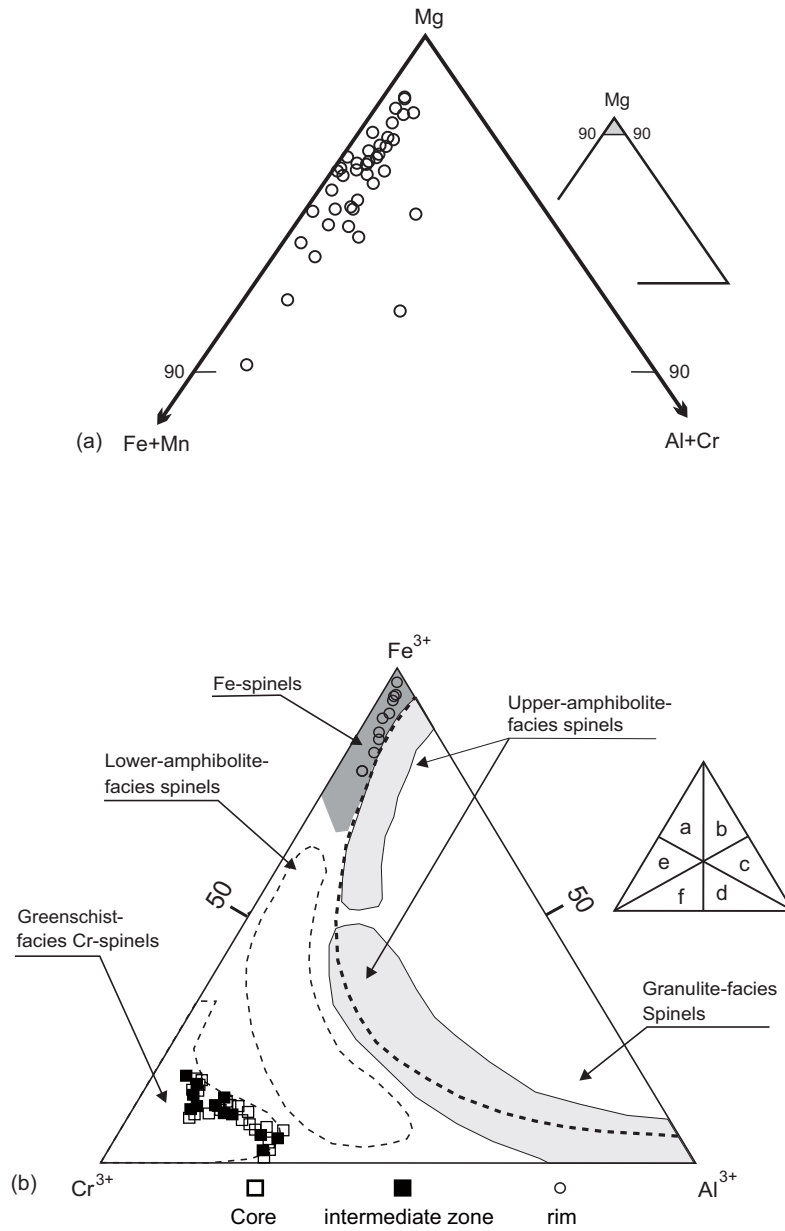


Fig. 4
 Abu-Alam and Hamdy (2013)
 Fluid interaction in the Arabian-Nubian Shield ophiolites

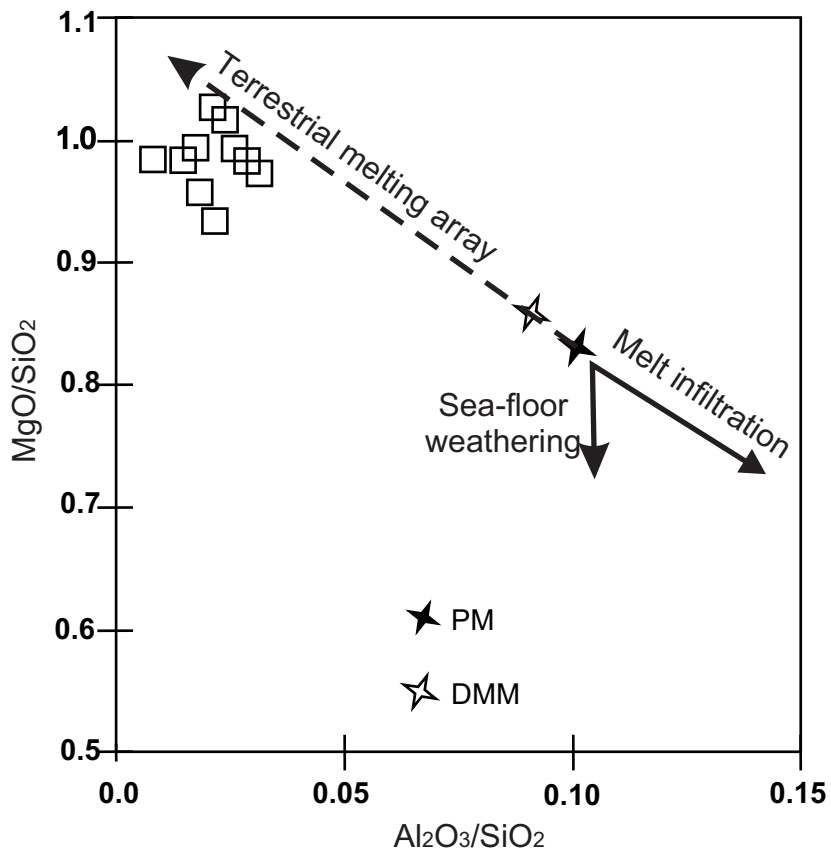


Fig. 5
Abu-Alam and Hamdy (2013)

Fluid interaction in the Arabian-Nubian Shield ophiolites

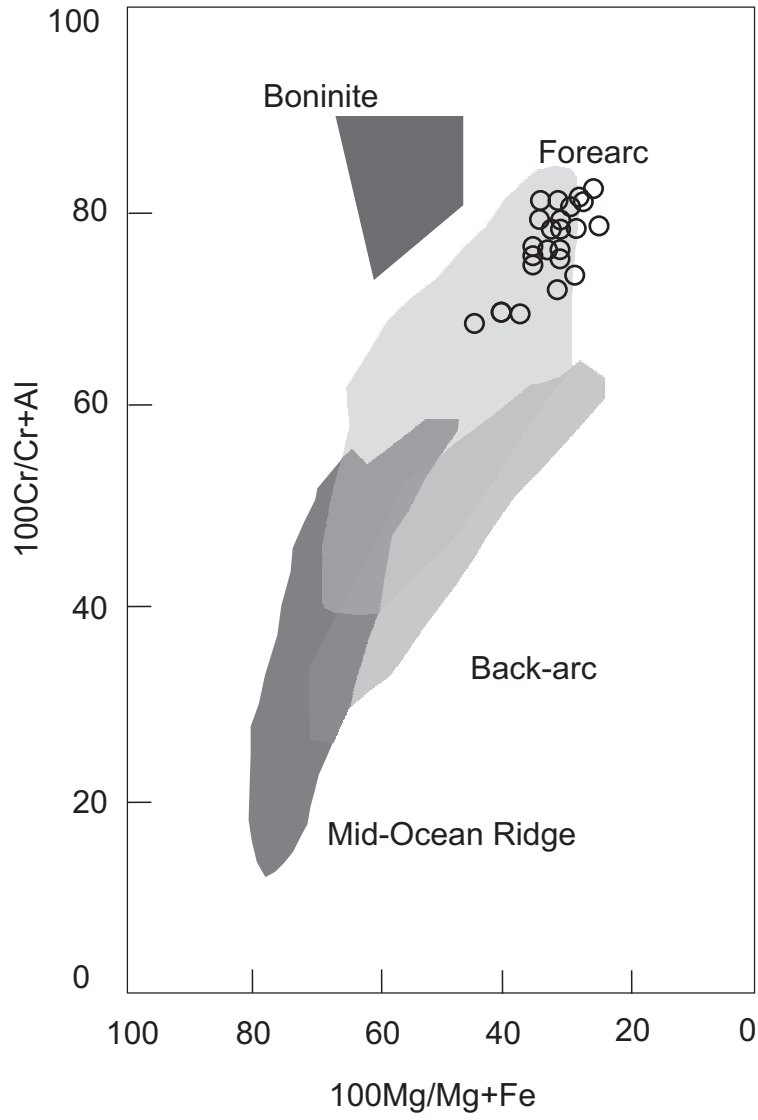


Fig. 6
Abu-Alam and Hamdy (2013)

Fluid interaction in the Arabian-Nubian Shield ophiolites

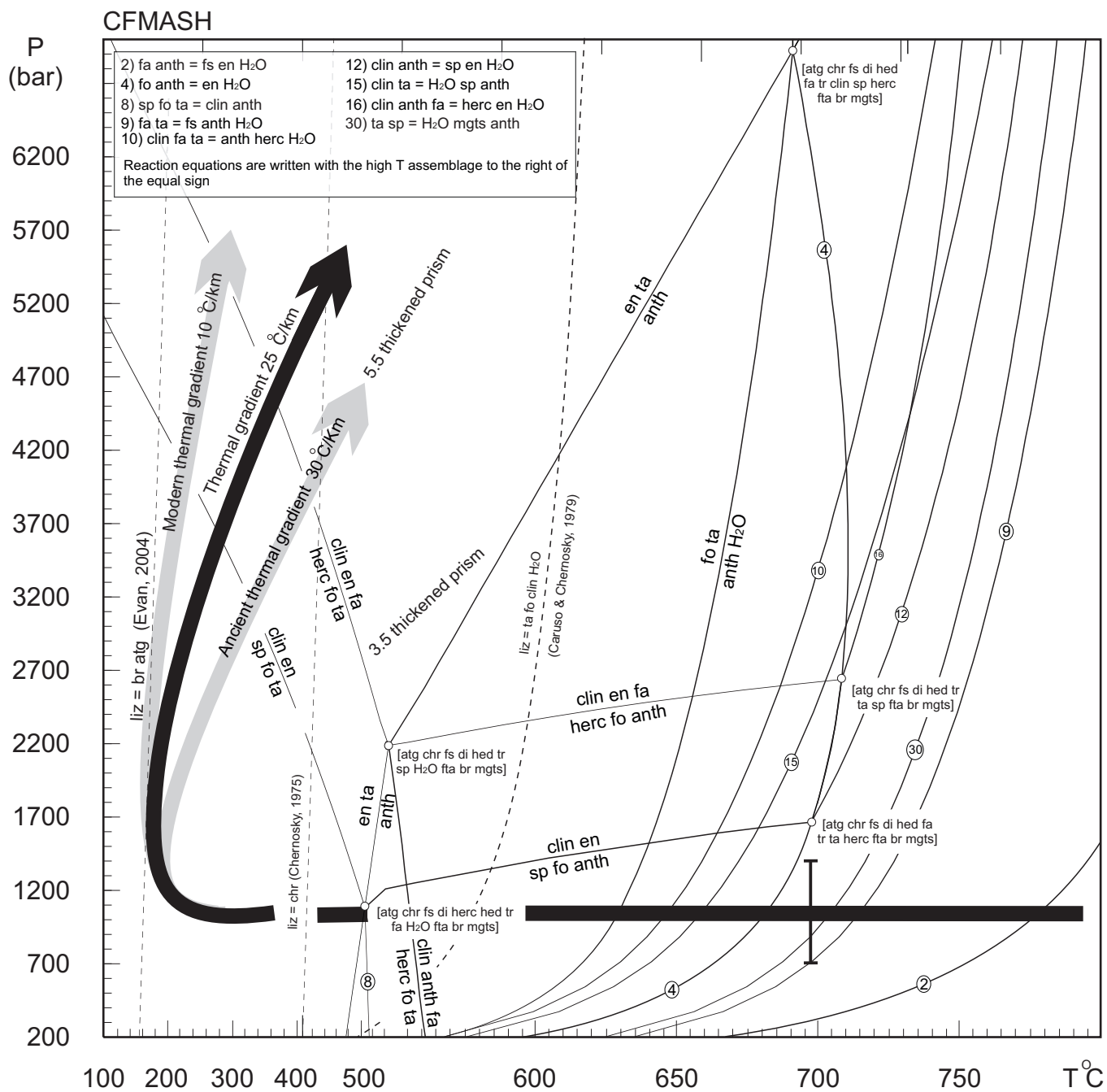


Fig. 8
Abu-Alam and Hamdy (2013)

Fluid interaction in the Arabian-Nubian Shield ophiolites

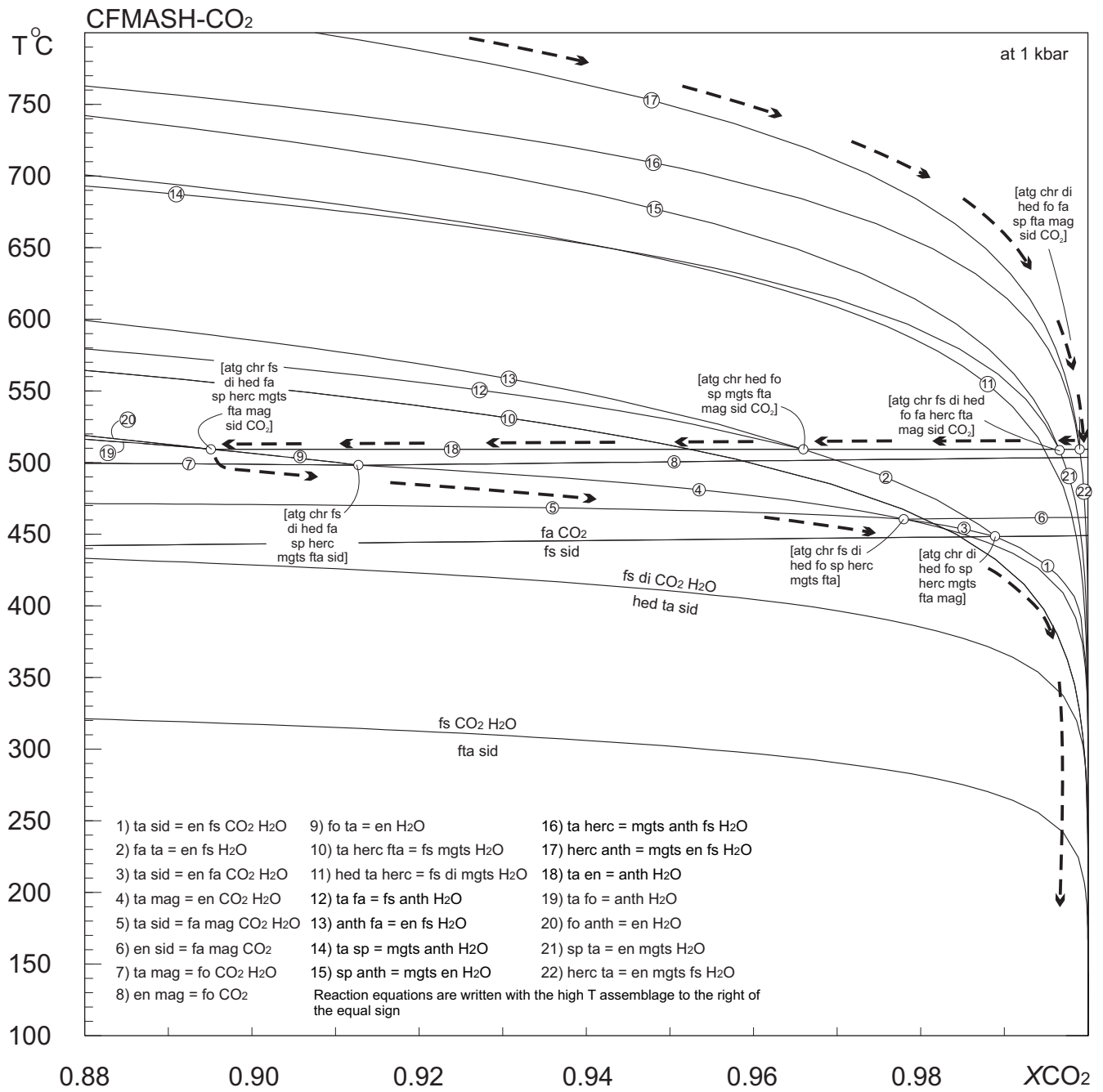


Fig. 9
Abu-Alam and Hamdy (2013)

Fluid interaction in the Arabian-Nubian Shield ophiolites

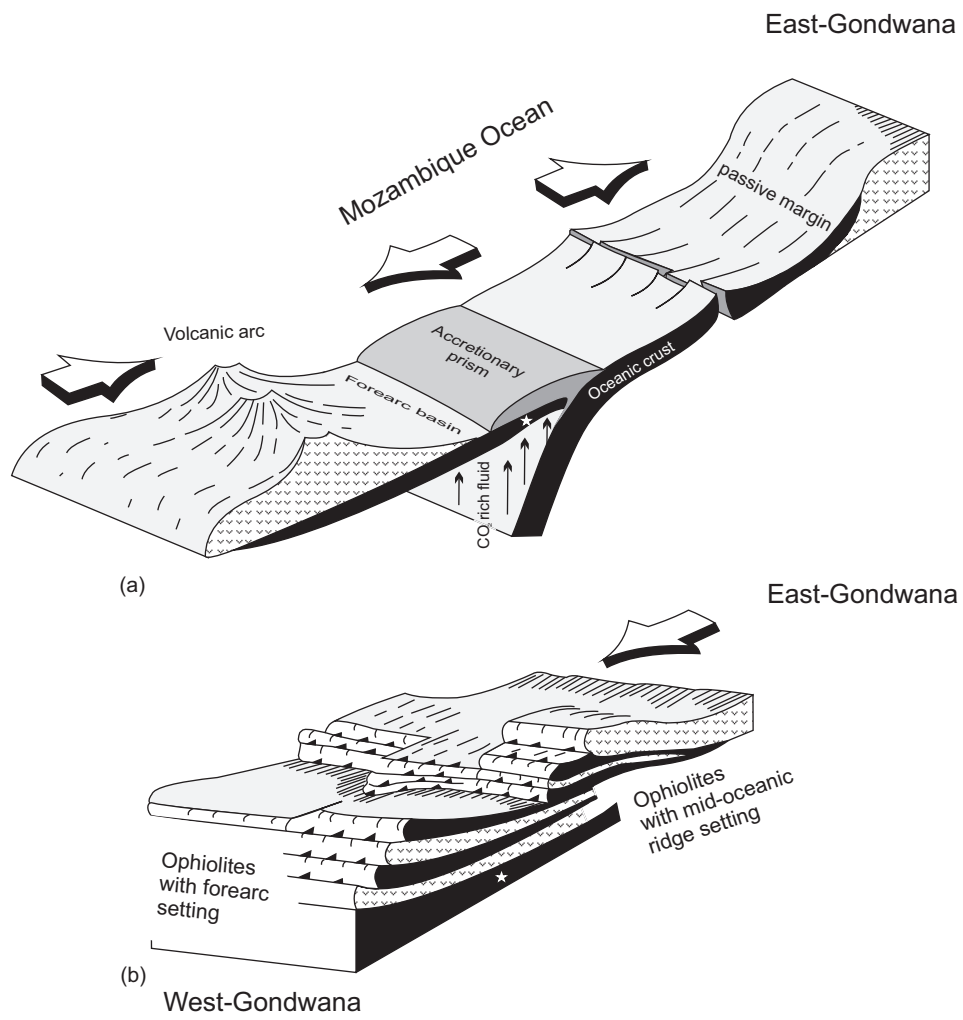


Fig. 10
Abu-Alam and Hamdy (2013)

Fluid interaction in the Arabian-Nubian Shield ophiolites